



# Evaluating the hydromechanical responses of seabed–pipelines with rotated anisotropic heterogeneous seabed properties

Zhengshou Lai <sup>a,b</sup>, Qiushi Chen <sup>c,\*</sup>, Linchong Huang <sup>d</sup>

<sup>a</sup> School of Intelligent Systems Engineering, Sun Yat-sen University, Shenzhen 518107, China

<sup>b</sup> Department of Civil and Environmental Engineering, The Hong Kong University of Science and Technology, Hong Kong, China

<sup>c</sup> Glenn Department of Civil Engineering, Clemson University, Clemson, SC 29634, USA

<sup>d</sup> School of Aeronautics and Astronautics Engineering, Sun Yat-sen University, Shenzhen 518107, China

## ARTICLE INFO

### Keywords:

Wave–seabed–pipeline interaction  
Hydromechanical responses  
Spatial variability  
Random field models  
Rotated anisotropy

## ABSTRACT

Seabed sediments are inherently heterogeneous and present different fabric patterns including rotated anisotropy. This work aims to investigate the effects of rotated anisotropy in seabed properties on the hydromechanical responses of seabed and pipelines. Rotated anisotropic seabed property fields (e.g., hydraulic conductivity and shear modulus fields) are generated using the random field theory, and are then coupled with finite element models to simulate the hydromechanical responses of seabed–pipelines under dynamic nonlinear wave-induced loadings. Monte Carlo simulations are performed to approach a probabilistic analysis of the effects of heterogeneous seabed fields. The pore pressure, liquefaction, seabed displacement, and pipeline stress are analyzed for systematic varying rotation angles. The results show that the upper bounds of the liquefied area would decrease by about 15% and 8% with increasing rotated anisotropy in the hydraulic conductivity and shear modulus fields, respectively. For rotated anisotropic shear modulus fields, the von Mises stress is minimum when the rotation angle is 45°. The transverse anisotropy in hydraulic conductivity or shear modulus is the most unfavorable situation, the results of which could be relied upon for a conservative design if the rotated anisotropy of a seabed property is unknown in a field project.

## 1. Introduction

Submarine pipelines have been widely used in offshore oil and gas exploitation and submarine transportation. A submarine pipeline, together with its surrounding seabed soils, form a seabed–pipeline system, whose hydromechanical responses could be rather complex under the influence of dynamic wave-induced loadings. One typical problem associated with a seabed–pipeline system is liquefaction (Sumer, 2014), a situation in which excess pore pressure builds up significantly and the seabed soil loses its strength (Ye and Wang, 2016; Yang and Ye, 2017, 2018). During liquefaction, the structural safety and serviceability of submarine pipelines begin to suffer. In view of the importance of submarine pipelines and the complexity of their hydromechanical responses, research on seabed–pipeline behavior has gained tremendous popularity among the petroleum, civil, and ocean engineering communities.

Generally, the behavior of a seabed–pipeline system is a coupled multi-physics process, which includes fluid flow processes (seawater) and solid deformations (seabed skeleton and pipeline). Thus far, the finite element method (FEM) has been shown to be a pre-eminent

numerical tool for solving such a coupled multi-physics problem (Jeng and Lin, 1999; Zhou et al., 2014; Zhang et al., 2016b; Tong et al., 2017). Many advanced FEM numerical models and tools, e.g., the DYNE3WAC (Ou, 2009), the Pastor–Zienkiewicz Mark III (Pastor et al., 2011), and the FSSI-CAS (Zhang et al., 2019), have been developed to simulate the complex hydromechanical response of seabed–pipeline system under the effects of seismic wave and current wave. In FEM-based seabed–pipeline analysis, the model responses are heavily influenced by the input parameters such as soil permeability, shear modulus, and degree of saturation. A comprehensive evaluation of the seabed–pipeline responses requires a complete characterization of the seabed soil properties. Seabed soils, however, are heterogeneous with different properties at different locations. Over the years, various models have been developed to characterize heterogeneous seabed soils, and these models can be grouped into three classes: (1) multi-regional models (Hsu et al., 1995; Zhou et al., 2011), in which the seabed is divided into a number of sub-regions with each sub-region being assumed to have uniform permeability, porosity, shear modulus, etc.; (2) trend models (Jeng and Seymour, 1997; Sui et al., 2018), which describe the

\* Corresponding author.

E-mail address: [qiushi@clemson.edu](mailto:qiushi@clemson.edu) (Q. Chen).

<https://doi.org/10.1016/j.oceaneng.2021.109226>

Received 21 November 2020; Received in revised form 29 March 2021; Accepted 22 May 2021

Available online 5 June 2021

0029-8018/© 2021 Elsevier Ltd. All rights reserved.

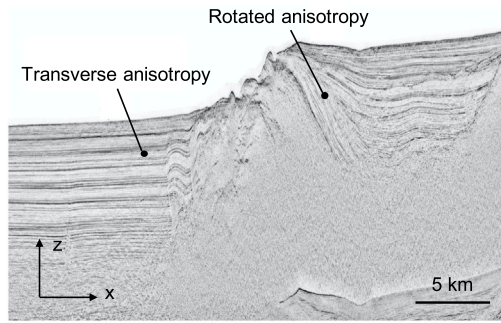


Fig. 1. Multi-channel seismic reflection profiles showing the layering profile of seabed sediment.

Source: The figure is modified from that in Walton et al. (2018).

seabed parameters using continuous depth-dependent functions; and (3) random field models (Zhang et al., 2016a; Lai et al., 2019), in which the seabed soil properties at every location are quantified as a set of random variables and the values of these variables are described by a joint probability distribution. These models can be combined as well (e.g., the multi-regional and trend-function model Zhang et al., 2016b; Sui et al., 2019, the trend-function and random field model Peng et al., 2017). Among these models, random field models can effectively capture and model the heterogeneous features of soil properties in nature, and thus, there has been an increasing interest in adopting random field models to characterize heterogeneous soils.

A number of studies have been carried out to investigate the effects of random field soil properties on the seabed responses. For example, Zhang et al. (2016a) considered the soil permeability, shear modulus, and degree of saturation as log-normally distributed random fields and input them into FEM models to simulate seabed responses. Zhu et al. (2019a) performed a reliability analysis to evaluate the stability of submarine slopes using the limit equilibrium method and coupled it with the random field theory to model the spatial variability in seabed strength. In the case that soil properties are not independent, simulations can be further developed with the cross-correlated random field method as in the work of Peng et al. (2017). However, it should be noted that these studies mainly focused on seabeds that have a horizontally deposited fabric pattern. That is, soil properties show smooth variations in the horizontal direction (i.e., the bedding orientation) and rapid variations in the vertical direction. In reality, soils, including seabed sediments, can exhibit different fabric patterns after processes such as deposition, self-weight compaction, and wave-induced loadings. Fig. 1 shows an example of the layering profile of seabed sediment constructed from multi-channel seismic reflection data. Depending on the correlation structure, the deposition profile of a soil field can be classified into six typical classes (Zhu and Zhang, 2013): isotropy, transverse anisotropy, rotated anisotropy, general anisotropy, general rotated anisotropy, and their combinations. In addition to transverse anisotropic seabeds analyzed in previous studies, rotated anisotropic seabeds are also commonly seen in nature (e.g., in coastal slopes) but remain a less-explored topic.

In the context of the random field theory, the extent of variations in a soil property along one direction can be characterized by the so-called scale of fluctuation (SOF). The directions in which the soil properties show smooth variations are generally quantified with larger SOF values, and vice versa. Usually, soil fabric, in the two-dimensional case, is directional with two principal directions, with the major principal direction having the largest SOF and the minor principal direction having the smallest SOF. For heterogeneous soils with transverse anisotropy, the principal directions in the fabric are parallel to the Cartesian coordinate axes, while for rotated anisotropic heterogeneous soils, the principal directions are rotated from the Cartesian coordinate axes by a certain angle. Griffiths et al. (2009) were

among the first to consider rotated anisotropic heterogeneous soils and investigate their effects on slope stability. Rotated anisotropic heterogeneous shear strength fields were generated by first generating transverse anisotropic random shear strength fields and then rotating them by the desired angle. In addition, in a recent work by Zhu et al. (2019b), extensive studies with parametric rotation angles were conducted to investigate how the fabric orientation of anisotropically deposited soil influences the stability and failure mechanism of a slope and to identify the critical fabric orientation that is most unfavorable to slope stability. Motivated by the pioneering work of Griffiths et al. (2009) and Zhu et al. (2019b), the objective of this study is to evaluate the hydromechanical responses of seabed-pipelines considering rotated anisotropic heterogeneous seabed properties and to identify the critical fabric orientation that is most unfavorable to the seabed and pipeline stability. This work builds on the previous effort (Lai et al., 2019), which studied the effects of spatially correlated seabed properties on the characteristic hydromechanical responses of seabed-pipeline, whereas this work puts an emphasis on the effects of rotated anisotropy in the seabed heterogeneity. Moreover, the nonlinear wave theory is implemented in this study, which is better suited to large-amplitude waves that are more relevant for seabed liquefaction.

The remainder of the paper is organized as follows. First, the methodology and simulation procedures of rotated anisotropic heterogeneous soil using the random field theory are presented in Section 2. Then, with the formulation of the coupled hydromechanical problem of seabed-pipeline and the framework of the probabilistic analysis described in Section 3, an illustrative example of seabed-pipeline is set up and analyzed in Section 4. In this example, the seabed hydraulic conductivity and shear modulus are considered heterogeneous with rotated anisotropy, and their effects on pore pressure, liquefaction, seabed displacement, and pipeline stress are investigated. Finally, concluding remarks are drawn in Section 5 based upon the results presented.

## 2. Random field seabed properties with rotated anisotropy

### 2.1. Correlation structure of rotated anisotropy

As mentioned above, soils, including seabeds, are inherently heterogeneous, with material properties showing different values at different locations. These values, however, are usually not completely independent but are spatially correlated with each other. The random field theory is an effective tool to model such spatially varying but correlated material properties, e.g., Chen et al. (2016b,a), Liu et al. (2017), Leung et al. (2018) and Shen et al. (2019). As a result of colluvium processes, topples, end-tipping construction, and other processes, the spatial distribution of a soil property could exhibit several typical fabric patterns, including isotropy, transverse anisotropy, rotated anisotropy, general anisotropy, general rotated anisotropy, and their combinations (Zhu and Zhang, 2013). Therefore, a rigorous framework for generating a random field with typical fabric patterns was proposed in Zhu and Zhang (2013) and is employed in this work for the simulation of heterogeneous seabed properties with preferred bedding orientations.

Within the random field theory, a material property at various locations is quantified as a set of random variables. Each random variable follows a probability distribution, and the relation between these random variables is characterized by a correlation function. Supposing that a random field is stationary, the probability distributions are constant for all locations, and the correlation function depends only on the separation distance regardless of the exact locations. The SOF in the correlation function characterizes the extent of the variations between random variables at adjacent locations. Soil properties exhibit a large SOF in the major principal direction and a small SOF in the minor principal direction. For rotated anisotropic heterogeneous soils, the major and minor principal directions are not parallel to the Cartesian coordinate axes. According to the framework proposed in Zhu and Zhang (2013), the correlation structure of rotated anisotropy, in the

two-dimensional case, can be characterized by an extended elliptical function

$$\rho(\Delta x, \Delta z) = \exp \left( -\sqrt{\left( \frac{\Delta x \cos \beta + \Delta z \sin \beta}{\theta_1} \right)^2 + \left( \frac{-\Delta x \sin \beta + \Delta z \cos \beta}{\theta_2} \right)^2} \right) \quad (1)$$

where  $\rho$  is the correlation between soil properties at two locations with separation distances  $\Delta x$  and  $\Delta z$  in the horizontal and vertical directions, respectively; parameters  $\theta_1$  and  $\theta_2$  are the SOFs in the major and minor principal directions, respectively;  $\beta$  is the rotational angle of the major principal direction from the  $x$ -axis. The correlation structure of rotated anisotropy in the three-dimensional case can be derived from an extended ellipsoidal function, and the interested reader is referred to Liu and Leung (2018).

## 2.2. Simulation procedures

With the correlation structure of a soil property, random fields of these soil properties could be generated using various algorithms, such as the moving average method (Cressie and Pavlicová, 2002), the local average subdivision method (Fenton and Vanmarcke, 1990), the covariance matrix decomposition method (Chenari and Farahbakhsh, 2015), and sequential simulation methods (Chen et al., 2012; Wang and Chen, 2018). In this paper, the covariance matrix decomposition method is adopted owing to its simplicity and computational efficiency. The simulation procedures are briefly described as follows, and the interested reader is referred to Davis (1987) and Sudret and Der Kiureghian (2000) for more details.

Step 1: discretize the field into a set of grid points, which are analogous to nodes in a finite element mesh and the grid can be structured or unstructured. Values of random field variables will be calculated at the grid locations.

Step 2: calculate the correlation matrix and perform covariance matrix decomposition. The correlation matrix, denoted by  $C$ , consists of components  $\rho_{ij}$ , which characterize the correlation between random variables at locations  $i$  and  $j$ , respectively. In this work, the correlation is calculated with Eq. (1) to reproduce the seabed fabric with rotated anisotropy. Using the Cholesky decomposition method, the correlation matrix is decomposed as  $C = LL^T$ , where the superscript  $T$  indicates the transpose of the matrix.

Step 3: generate a random field of standard normally-distributed variables  $Z$ . With reference to the covariance matrix decomposition method, a random field of the normalized variable  $Z$  could be sampled from Davis (1987)

$$Z = LU \quad (2)$$

where  $U$  is a vector of independent random variables obeying a standard normal distribution.

Step 4: transform the standard normally-distributed variables  $Z$  to a specific distribution. For a soil property  $S$  that obeys a general normal distribution, it can be obtained from a standard normal distribution by first multiplying the standard deviation and then adding the mean, such that

$$S = \mu_s + Z\sigma_s \quad (3)$$

where  $\mu_s$  and  $\sigma_s$  are the mean and standard deviation, respectively, of soil property  $S$ , and  $Z$  is the normalized variable. For log-normally distributed soil properties, the transformation is given as

$$S = \exp(\mu_{\ln s} + \sigma_{\ln s} Z) \quad (4)$$

where  $\mu_{\ln s}$  and  $\sigma_{\ln s}$  are the mean and standard deviation, respectively, of the logarithmic variable  $S$  (i.e.,  $\ln S$ ) such that

$$\sigma_{\ln s} = \sqrt{\ln [1 + (\sigma_s / \mu_s)^2]} \quad (5)$$

$$\mu_{\ln s} = \ln \mu_s - \frac{1}{2} \sigma_{\ln s}^2 \quad (6)$$

where  $\mu_s$  and  $\sigma_s$  are the mean and standard deviation, respectively, of variable  $S$ . In case that soil properties obey other distributions, such as a Weibull distribution (Weibull, 1951; Lai et al., 2003), the transformation can be approached by performing a normal score mapping (Chen et al., 2012).

## 3. Probabilistic hydromechanical analysis of seabed-pipelines

With heterogeneous seabed properties generated using the random field theory, stochastic hydromechanical analysis of seabed-pipeline can be performed, and the seabed-pipeline responses could be analyzed probabilistically. A simple seabed-pipeline system consists of a porous seabed and an embedded pipeline. In this work, the coupled hydromechanical FEM model previously developed in Zhou et al. (2014) is adopted for the hydromechanical analysis of seabed-pipeline. For completeness, the model formulation, as well as the framework for the probabilistic analysis of seabed-pipeline responses, is briefly described in this section. For the detailed implementation and validation tests of the adopted hydromechanical FEM model, the interested reader is referred to Zhou et al. (2014) and Lai et al. (2019).

### 3.1. Formulation of the hydromechanical model

The seabed-pipeline system is modeled as a plane strain problem by neglecting the deformation along the longitudinal direction of the pipeline. Elastic constitutive relations are assumed for both the seabed solid skeleton and the pipeline. Concerning the seabed, the final governing equations, derived from the balances of mass and linear momentum, are written as follows (Zhou et al., 2014; Lai et al., 2019):

$$K_x \frac{\partial^2 p}{\partial x^2} + K_z \frac{\partial^2 p}{\partial z^2} - \phi_f \rho_f g \beta_f \frac{\partial p}{\partial t} = -\rho_f \frac{\partial^2}{\partial t^2} (K_x \frac{\partial u}{\partial x} + K_z \frac{\partial w}{\partial z}) + \rho_f g \frac{\partial}{\partial t} (\frac{\partial u}{\partial x} + \frac{\partial w}{\partial z}) \quad (7)$$

$$\frac{\partial p}{\partial x} = -\rho \frac{\partial^2 u}{\partial t^2} + G_s (\frac{\partial^2 u}{\partial x^2} + \frac{\partial^2 w}{\partial z^2}) + \frac{1}{1-2\nu_s} G_s \frac{\partial}{\partial x} (\frac{\partial u}{\partial x} + \frac{\partial w}{\partial z}) + \rho b_x \quad (8)$$

$$\frac{\partial p}{\partial z} = -\rho \frac{\partial^2 w}{\partial t^2} + G_s (\frac{\partial^2 w}{\partial x^2} + \frac{\partial^2 u}{\partial z^2}) + \frac{1}{1-2\nu_s} G_s \frac{\partial}{\partial z} (\frac{\partial u}{\partial x} + \frac{\partial w}{\partial z}) + \rho b_z \quad (9)$$

where  $u$  and  $w$  are the horizontal ( $x$ ) and vertical ( $z$ ) displacements, respectively;  $p$  is the excess pore pressure;  $K_x$  and  $K_z$  are the seabed hydraulic conductivity in the horizontal and vertical directions, respectively;  $G_s$  is the seabed shear modulus;  $\nu_s$  is the seabed Poisson's ratio;  $\phi_f$  is the void volume fraction of the seabed;  $\rho_f$  is the intrinsic mass density of the fluid (i.e., seawater in this case);  $\rho$  is the equivalent density of the seabed and pore fluid;  $g$  is the gravitational acceleration;  $b_x$  and  $b_z$  are the  $x$  and  $z$  components of the body force. The parameter  $\beta_f$  accounts for both the compressibility of the pore fluid and the degree of saturation of the porous seabed and is given as (Ülker, 2015; Liao et al., 2018)

$$\beta_f = \frac{1}{k_f} + \frac{1 - S_r}{p_{f0}} \quad (10)$$

where  $S_r$  is the degree of saturation;  $k_f$  is the bulk modulus of the fluid and  $p_{f0}$  is the static pore pressure, which is calculated as  $p_{f0} = p_a + \rho_f g d$ , where  $p_a = 10^5$  Pa is the atmospheric pressure and  $d$  is the water depth. It should be noted that in the governing Eqs. (7), (8) and (9), the spatial derivative terms of the non-homogeneous seabed soil properties (e.g., the hydraulic conductivity  $K_x$  and  $K_z$ , the shear modulus  $G_s$ ) are not involved. In the random field approach, soil properties are characterized by discrete values. The spatial derivatives of a random field property (i.e., discrete values) are not well-defined and thus are not considered in this study. In addition, seabed soil in a real offshore environment is often loosely deposited soil with complex nonlinear, inelastic, and history-dependent behavior. As the focus of this study is on the effects of rotational anisotropy in seabed properties, an elastic

constitutive model is adopted for the seabed soil. Examples of more sophisticated constitutive models of seabed soil can be found in Pastor et al. (2011) and Zhao et al. (2016, 2017), and will be explored in future work.

For the pipeline, the final governing equations are derived from the balance of linear momentum and are written as

$$-\rho_p \frac{\partial^2 u}{\partial t^2} + G_p \left( \frac{\partial^2 u}{\partial x^2} + \frac{\partial^2 u}{\partial z^2} \right) + \frac{1}{1-2\nu_p} G_p \frac{\partial}{\partial x} \left( \frac{\partial u}{\partial x} + \frac{\partial w}{\partial z} \right) + \rho_p b_x = 0 \quad (11)$$

$$-\rho_p \frac{\partial^2 w}{\partial t^2} + G_p \left( \frac{\partial^2 w}{\partial x^2} + \frac{\partial^2 w}{\partial z^2} \right) + \frac{1}{1-2\nu_p} G_p \frac{\partial}{\partial z} \left( \frac{\partial u}{\partial x} + \frac{\partial w}{\partial z} \right) + \rho_p b_z = 0 \quad (12)$$

where  $G_p$  is the pipeline shear modulus,  $\nu_p$  is Poisson's ratio of the pipeline, and  $\rho_p$  is the density of the pipeline.

Based on the coupled partial differential equations defined by Eqs. (7), (8), (9), (11), and (12), the hydromechanical responses of seabed-pipeline can be solved. In this work, COMSOL Multiphysics software with the *LiveLink for MATLAB* interface is adopted to implement and solve the partial differential equations. In particular, the *General Form PDE interface* in COMSOL is used to customize these partial differential equations. The hydromechanical FEM model is first set up within COMSOL Desktop and then exported as a MATLAB script, which can be easily integrated with the MATLAB codes for generating random field seabed properties.

### 3.2. Framework of the probabilistic analysis

As seabeds are considered heterogeneous, probabilistic analysis is utilized to obtain a comprehensive characterization of the seabed-pipeline behavior. The framework of probabilistic analysis of the seabed-pipeline hydromechanical responses consists of three main components: (1) with the statistics (i.e., the mean, variance, and scale of fluctuation) of a seabed property, heterogeneous property fields are generated using the random field theory; (2) the hydromechanical FEM model of seabed-pipeline is set up with the generated random field seabed properties taken as the input, and the seabed-pipeline responses are solved and analyzed; and (3) with the aid of Monte Carlo simulation (MCS), the seabed-pipeline responses are solved repeatedly with different realizations of random field seabed properties. The matrices of interest (e.g., the excess pore pressure, liquefaction zone, pipeline displacements or stress) are analyzed statistically. It should be noted that in component (2), the hydromechanical FEM model requires the seabed properties at the locations of Gaussian points of each element. To integrate the random field seabed properties into the FEM model, one option is to directly simulate the seabed properties at the Gaussian points, as in Lai et al. (2019). Another option is to first simulate the seabed properties at a set of grid points that cover the entire seabed domain and then interpolate the seabed properties at the Gaussian points using algorithms such as the nearest neighbor interpolation or linear interpolation. The second option is simple to implement and efficient for FEM models with a large number of nodes. In this work, the second option with linear interpolation is adopted.

## 4. Numerical examples

To investigate the effects of heterogeneous seabed properties with rotated anisotropy on seabed-pipeline behavior, an example of a rectangle seabed with an embedded circular (cross-section) pipeline is studied in this section. This example has previously been studied in Lai et al. (2019), where the effects of spatially correlated seabed properties on the characteristic hydromechanical responses of seabed-pipeline, including parametric studies of the random field parameters (e.g., coefficient of variation (COV) and scale of fluctuation (SOF)), have been analyzed. As an extension of that study, this work further analyzes the effects of rotated anisotropy on the seabed properties.

### 4.1. Model set-up

#### 4.1.1. Geometries and boundary conditions

The seabed, as shown in Fig. 2, is 100 m wide and 30 m deep. The pipeline is buried 2 m below the seabed surface with a diameter of 1 m and a thickness of 0.05 m. With regard to the boundary conditions of the seabed, for the solid phase (with respect to the degree of freedom  $u$  and  $w$ ), the bottom of the seabed is fixed with no displacements, the lateral sides are constrained with rollers (i.e., no horizontal displacements), and the top surface is free. For the fluid phase (with respect to the degree of freedom  $p$ ), both the seabed bottom and lateral sides are specified with no flux, while the seabed surface is subject to dynamic wave pressure. In this work, the wave pressure  $p_b(t)$  is approximated by a third-order Stokes' solution, given by Hsu et al. (2009) and Ye and Jeng (2012)

$$p_b(x, t) = \frac{\rho_f g H}{2 \cosh \lambda d} \left[ 1 - \frac{\omega_2 \lambda^2 H^2}{2(U_0 \lambda - \omega_0)} \right] \cos(\lambda x - \omega t) + \frac{3\rho_f H^2}{8} \left[ \frac{\omega_0(\omega_0 - U_0 \lambda)}{2 \sinh^4 \lambda d} - \frac{g \lambda}{3 \sinh 2 \lambda d} \right] \cos(2(\lambda x - \omega t)) + \frac{3\rho_f \lambda H^3 \omega_0(\omega_0 - U_0 \lambda)}{512} \frac{(9 - 4 \sinh^2 \lambda d)}{\sinh^7 \lambda d} \cos(3(\lambda x - \omega t)) \quad (13)$$

where  $\rho_f$  is the seawater density;  $g$  is the gravity acceleration;  $d$  is the water depth;  $H$  is the wave height;  $\lambda = 2\pi/L$  is the wave number, where  $L$  is the wavelength;  $\omega = 2\pi/T$  is the wave frequency, where  $T$  is the wave period;  $U_0$  is the current velocity; and  $\omega_0$  and  $\omega_2$  is the first-order and third-order frequency, respectively. The wave frequency, wave number, and wave height are correlated through the dispersion relationship, given by

$$\omega = \omega_0 + (\lambda H)^2 \omega_2 \quad (14)$$

$$\omega_0 = U_0 \lambda + \sqrt{g \lambda \tanh \lambda d} \quad (15)$$

$$\omega_2 = \frac{9 + 8 \sinh^2 \lambda d + 8 \sinh^4 \lambda d}{64 \sinh^4 \lambda d} (\omega_0 - U_0 \lambda) \quad (16)$$

The wave-induced loading on the seabed skeleton is rather complicated due to the changeable interactions between the wave and seabed and is ignored in this work for simplicity. In fact, the wave-induced loadings on the seabed skeleton decreases as the depth to seabed increases (Yamamoto and Suzuki, 1980). With regard to the boundary conditions of the pipeline, its inner circumferential face is free, and its outer circumferential face is assumed to be perfectly bonded with the seabed; i.e., the seabed and the pipeline have the same displacements and the same stresses at the seabed-pipeline interface. No body force, including the gravity, is considered in the FEM simulations, and thus, the seabed-pipeline responses represent the net effects that are induced by the dynamics wave pressure. This is acceptable for elastic seabed; however, it should be noted that the gravity would affect the seabed-pipeline responses, and thus, should be taken into consideration if an elastoplastic soil model is adopted.

#### 4.1.2. Model parameters

Input parameters for the example seabed-pipeline problem are listed in Table 1. It should be noted that the adopted wave parameters correspond to a fairly large wave, representing a fairly extreme environment that may be encountered by the seabed-pipeline system. Nevertheless, based on the review in Maâtoug and Ayadi (2016), the adopted wave parameters are within the applicability range of the adopted third-order Stokes' solution (i.e., Eq. (13)). Also, no current is considered in the waves. The total simulation time is set to 16 s so that the seabed-pipeline responses after two complete waves can be captured. The seabed hydraulic conductivity and shear modulus are spatially-correlated variables with rotated anisotropy and are generated by following the random field simulation procedures presented in Section 2. In this work, the statistical characteristics (i.e., the mean, COV, and SOF) of a seabed soil property are chosen based on



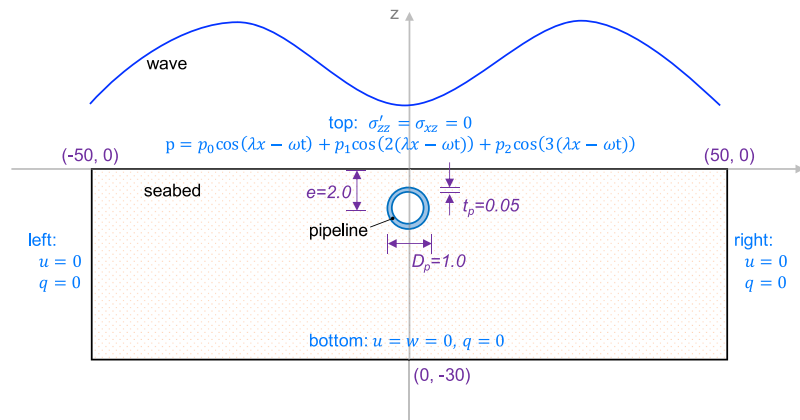


Fig. 2. Sketch of the example seabed–pipeline problem showing the geometric (units: m) and boundary conditions.

Table 1

Input parameters for the example seabed–pipeline hydromechanical problem.

Category	Parameter	Value	References
Seabed	Bulk density ( $\rho$ , kg/m <sup>3</sup> )	1790	Refs. Zhang et al. (2016a) and Peng et al. (2017)
	Hydraulic conductivity <sup>a</sup> ( $K_x$ , $K_z$ , m/s)	$5.0 \times 10^{-4}$	Ref. Zhang et al. (2016a)
	Shear modulus <sup>a</sup> ( $G_s$ , MPa)	10	Ref. Zhang et al. (2016a)
	Degree of saturation ( $S_r$ )	0.975	Ref. Zhang et al. (2016a)
	Poisson's ratio ( $\nu_s$ )	0.4	Ref. Zhou et al. (2014)
	Porosity ( $\phi_f$ )	0.4	Ref. Zhou et al. (2014)
Seawater	Density ( $\rho_f$ , kg/m <sup>3</sup> )	1030	Ref. Sharqawy et al. (2010)
	Bulk modulus ( $k_f$ , MPa)	$2.0 \times 10^3$	Ref. Sharqawy et al. (2010)
Pipeline	Density ( $\rho_p$ , kg/m <sup>3</sup> )	2700	Ref. Lai et al. (2019)
	Shear modulus ( $G_p$ , MPa)	$6.8 \times 10^4$	Ref. Lai et al. (2019)
	Poisson's ratio ( $\nu_p$ )	0.32	Ref. Lai et al. (2019)
Wave	Wave height ( $H$ , m)	6	Ref. Zhou et al. (2014)
	Water depth ( $d$ , m)	10	Ref. Zhou et al. (2014)
	Period ( $T$ , s)	8	Ref. Zhou et al. (2014)
	Wavelength ( $L$ , m)	81.42	Eq. (15)
	Current velocity ( $U_0$ , m/s)	0	–
Other	Gravitational acceleration ( $g$ , m/s <sup>2</sup> )	9.81	–
	Total simulation time (s)	16	–

<sup>a</sup>Note that the parameters take the specific values in the table for deterministic studies, and take random field values for probabilistic studies.

typical ranges recommended in previous research in the literature. Specifically, Rehfeldt et al. (1992) suggested that the vertical SOF of hydraulic conductivity is in 0.8~1.6 m, and the horizontal SOF is in 4.8~12.8 m. Jiang et al. (2014) recommended that the vertical SOF of shear modulus is in 0.5~3.0 m, and the horizontal SOF is in 10~40 m. While researches on the statistical characteristics of seabed soil properties are relatively limited, the interested reader is referred to Zhang et al. (2016a) and Lai et al. (2019) for a brief review. Results of the parametric studies on the COV and SOF have also been reported in Lai et al. (2019). In this example, both the hydraulic conductivity and the shear modulus are assumed to obey log-normal distributions. The hydraulic conductivity has a mean value of  $5.0 \times 10^{-4}$  m/s and a COV of 2.5, and the mean and COV for the shear modulus are 10 MPa and 0.45, respectively. The SOFs are assumed to be 20 m in the major principal direction and 1 m in the minor principal direction. For the rotation angle  $\beta$ , a parametric set of values ranging from 0° to 90° (half of 180° due to symmetry) is considered, which is sufficient for a comprehensive understanding of the effects of rotated anisotropy on seabed–pipeline behavior. It is worth noting that in offshore practices, the trenching and backfilling may be involved and can disturb the soil around a buried pipe significantly. The trenching and backfilling are not considered in this work.

#### 4.1.3. Simulation scenarios

Three sets of simulations are considered: (I) a probabilistic case in which the hydraulic conductivity is assumed to be heterogeneous

and the shear modulus is homogeneous; (II) a probabilistic case in which the shear modulus is heterogeneous and the hydraulic conductivity is homogeneous; and (III) a deterministic case in which both the seabed hydraulic conductivity and shear modulus are homogeneous. The deterministic case is used for comparison. Regarding the probabilistic cases, the seabed–pipeline problem is solved repeatedly for 500 times with 500 different realizations of the random fields. It should be noted that in reality, both the hydraulic conductivity and shear modulus could be heterogeneous with cross-correlations in between (Zhang et al., 2016a; Peng et al., 2017). In this example, the heterogeneity of the hydraulic conductivity and of the shear modulus is not incorporated concurrently, so that the effects of rotated anisotropic heterogeneous hydraulic conductivity and shear modulus can be investigated independently.

#### 4.2. Effects of rotated anisotropic hydraulic conductivity field

The probabilistic case in which only the hydraulic conductivity is heterogeneous is studied in this section. Following the random field simulation procedures provided in Section 2 and based on the statistics described in the previous section, rotated anisotropic heterogeneous hydraulic conductivity fields are generated first. To generate these fields, the domain is discretized into a number of  $200 \times 60$  ( $x$  by  $z$ ) elements, with each element having a length of 0.5 m. Therefore, one heterogeneous hydraulic conductivity field would consist of  $200 \times 60$  values. It is worth noting that there is a relationship that SOF and the

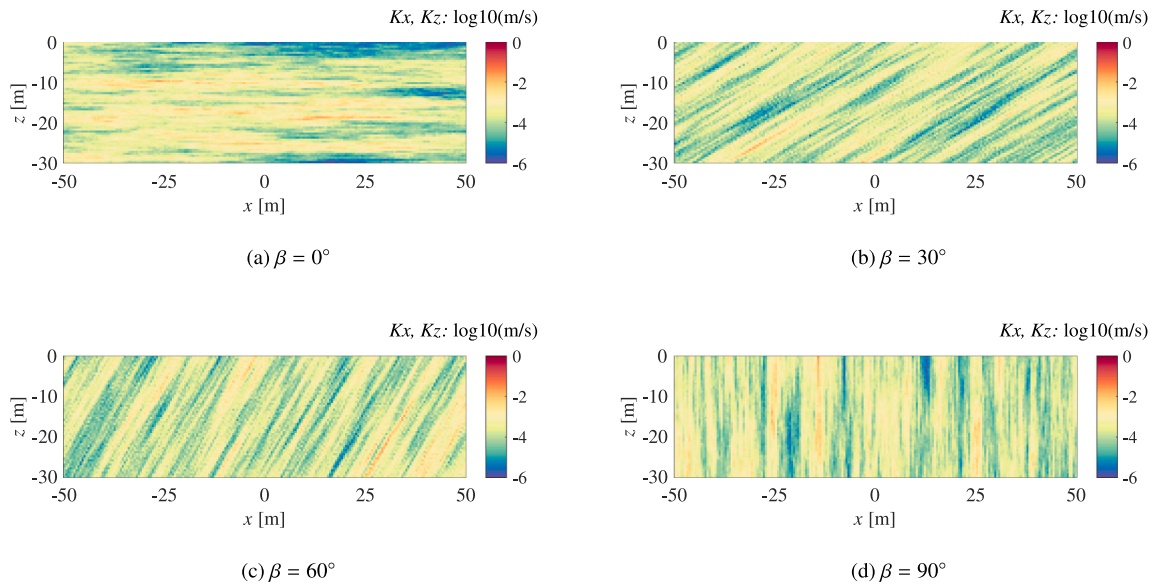


Fig. 3. Typical random field realizations of the heterogeneous hydraulic conductivity fields with different rotation angles.

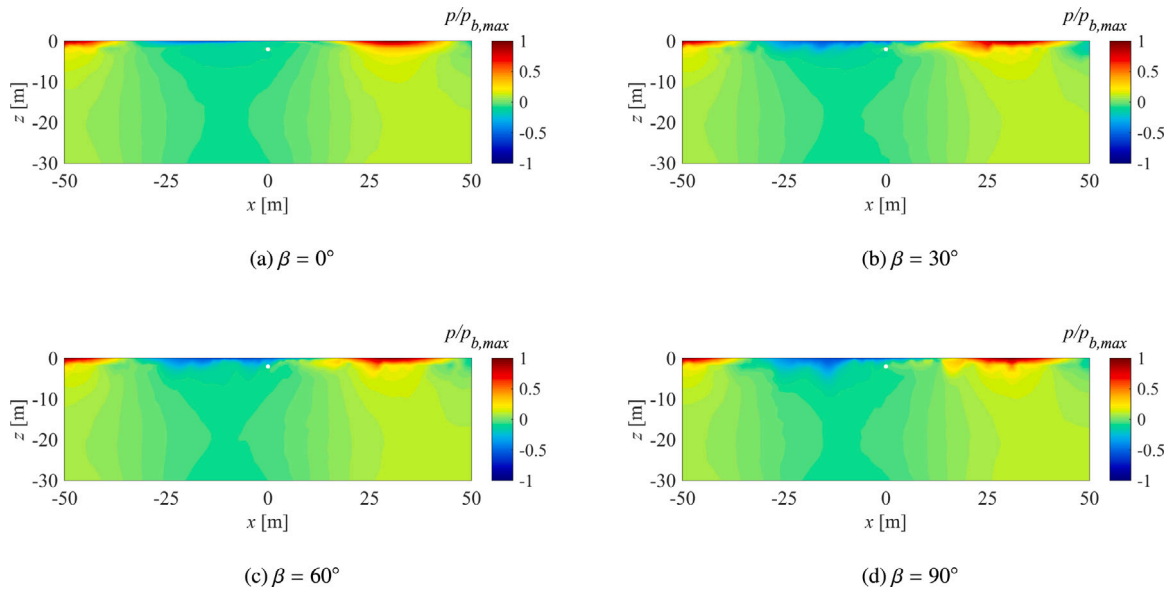


Fig. 4. Contours of the normalized excess pore pressure fields at time  $t = 3$  s for the cases of heterogeneous hydraulic conductivity fields with different rotation angles.  $p_{b,max}$  represents the maximum value of wave pressure.

element length of a random field mesh should be satisfied to achieve an acceptable discretization accuracy. Previous research (e.g., [Sudret and Der Kiureghian, 2000](#); [Allaix and Carbone, 2009](#)) has suggested that the element length is between  $1/4 \sim 1/2$  of SOF. Typical realizations of the random hydraulic conductivity fields with different rotation angles are shown in [Fig. 3](#). As the random fields are given distinct SOF values in the major and minor principal directions (i.e., 20 m and 1 m, respectively), the generated hydraulic conductivity fields exhibit clear layered profiles as expected. In addition, the bedding orientations of these hydraulic conductivity fields are consistent with the desired rotation angles. Although the hydraulic conductivity is taken as identical in the  $x$  and  $z$  directions, the anisotropy exists as a result of different SOF values in the major and minor principal directions and the spatially averaging effects.

With the generated random hydraulic conductivity fields taken as input, the coupled hydromechanical problem is solved, and the seabed–pipeline responses are analyzed probabilistically. Of particular interest,

the results of (1) pore pressure and liquefaction, (2) seabed displacements, and (3) pipeline stresses are presented in the following. It should be noted that the mesh used in the FEM is not necessary to be the same as the mesh used in random field generation. In this example, the mesh in the FEM consists of triangular elements with dense elements within the vicinity of the pipeline.

#### 4.2.1. Pore pressure and liquefaction

First, the pore pressure and liquefaction situations of the seabed are analyzed. [Fig. 4](#) shows the contours of the normalized excess pore pressure fields at time  $t = 3$  s for the cases of heterogeneous hydraulic conductivity fields with different rotation angles. Note that, unless otherwise noted, the contours presented in the following represent the results of one typical MCS, which corresponds to the random field realizations previously shown in [Fig. 3](#). At this particular time (i.e.,  $t = 3$  s), the pipeline is close to a wave trough, a situation in which the seabed soil around the pipeline would have a high potential to liquefy

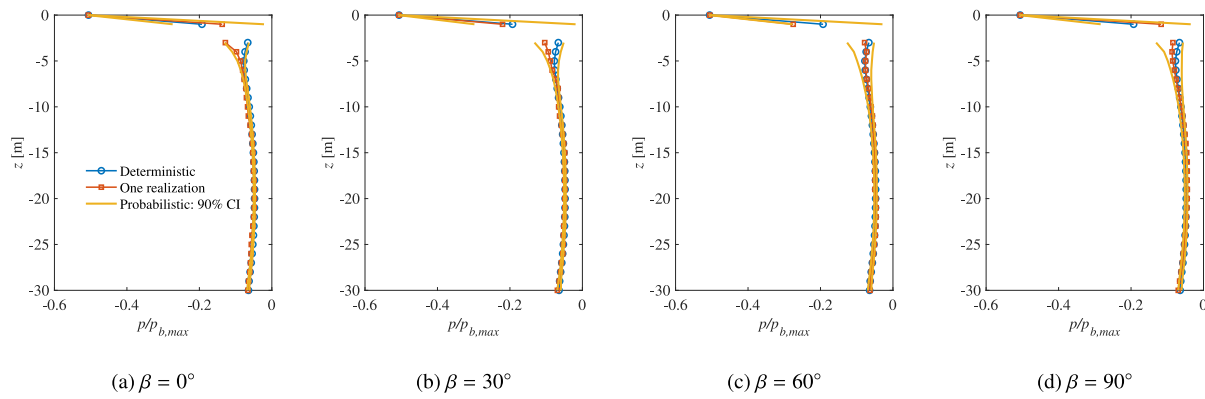


Fig. 5. Distributions of the excess pore pressure along the vertical cutline  $x = 0$  at time  $t = 3$  for the heterogeneous hydraulic conductivity fields (90% confidence interval shown) with different rotation angles. Results of the deterministic case and of one typical realization of the probabilistic case are also plotted as comparisons.

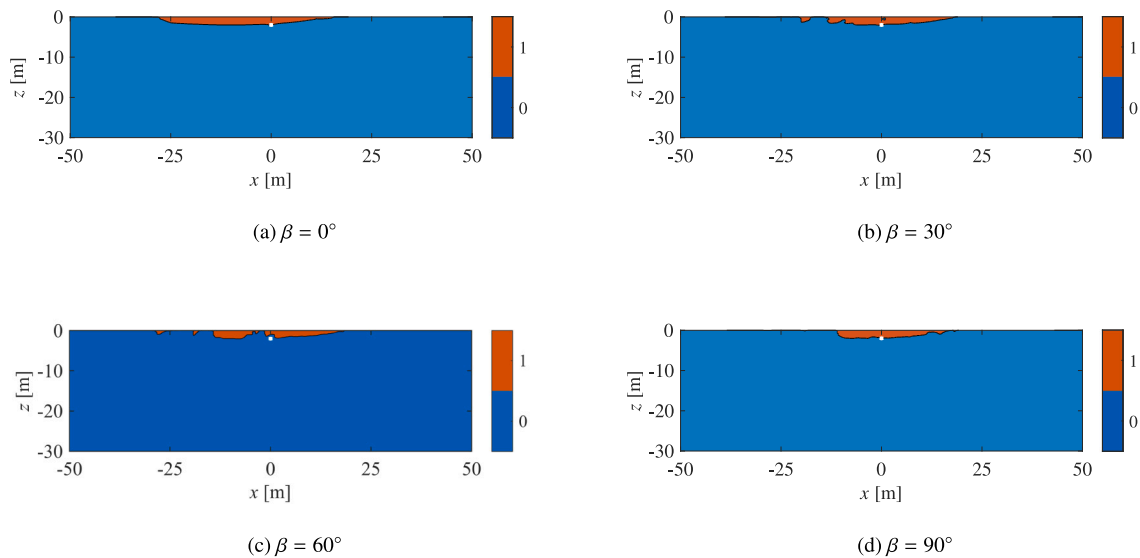


Fig. 6. Contours of the liquefaction fields at time  $t = 3$  s for the cases of heterogeneous hydraulic conductivity fields with different rotation angles (“1” corresponds to liquefaction and “0” to non-liquefaction).

(as will be illustrated later). The excess pore pressure is normalized with respect to the amplitude of the wave-induced pressure so that one can obtain a more direct sense of the pore pressure build-up and dissipation situations in the seabed. Overall, the excess pore pressure fields in these four cases (i.e.,  $\beta = 0^\circ$ ,  $30^\circ$ ,  $60^\circ$ , and  $90^\circ$ ) exhibit similar patterns. The region under the wave troughs experiences negative excess pore pressure, while the region under wave crests experiences positive values. The magnitudes of the excess pore pressure peak near the seabed surface and decrease quickly with depth.

To gain a quantitative insight into the effects of rotated anisotropy on pore pressure, the excess pore pressure along a vertical cutline ( $x = 0$  m and  $z$  from  $-30$  m to  $0$  m) is probed. At this time, the results of the 500 MCSs are analyzed altogether. Fig. 5 plots the 90% confidence interval of the normalized excess pore pressure, together with the results of the deterministic case and of one MCS, at time  $t = 3$  s. For all the rotation angles, the normalized excess pore pressure (in magnitude) decreases quickly from approximately 0.5 to 0.07 with depth going from  $0$  m to  $-2.5$  m (i.e., the depth of the bottom of the pipeline), and the excess pore pressure varies mildly below this depth. The uncertainty in the excess pore pressure, which is due to soil heterogeneity, increases with depth and then vanishes at a depth below the pipeline.

With the results of pore pressure, the liquefaction state at every location of the seabed can be evaluated. In this work, the transient

liquefaction criterion is adopted as follows (Zen and Yamazaki, 1990; Ye, 2012; Peng et al., 2017):

$$-(\rho - \rho_f)gz + p_b(x, t) - p(x, z, t) \leq 0 \quad (17)$$

where  $p_b(x, t)$  is the dynamic wave pressure defined in Eq. (13) and  $p(x, z, t)$  is the excess pore pressure at the location  $(x, z)$  and time  $t$ . If criterion (17) is met, the seabed is considered liquefied. It should be noted that the liquefaction criterion (17) is an indirect criterion by assuming constant total stress in the seabed soil. The total stress in seabed soil could change due to the complex soil and structure interaction effect, which has been studied in Ye and Wang (2015, 2016). Moreover, using a case study of a poroelastic seabed and the analytical solution for wave-induced excess pore-pressure, Qi and Gao (2018) showed that the pore pressure-based liquefaction criterion could lead to an unrealistic upward resultant force, which leads to tensile stresses in liquefied non-cohesive soil layer (Zhou et al., 2020). These two aspects are not considered in this work. It should also be noted that the installation process, as well as the structure weight, of the pipeline may also have an influence on the material properties and effective stresses of the surrounding seabed, and thus, affect the liquefaction depth of the seabed (Sui et al., 2017). In this work, the effects of stress changes in the seabed due to the installation and structure weight of the pipeline are not considered. Contours of the liquefaction fields at time  $t = 3$  s are shown in Fig. 6. At this particular time, the seabed soils

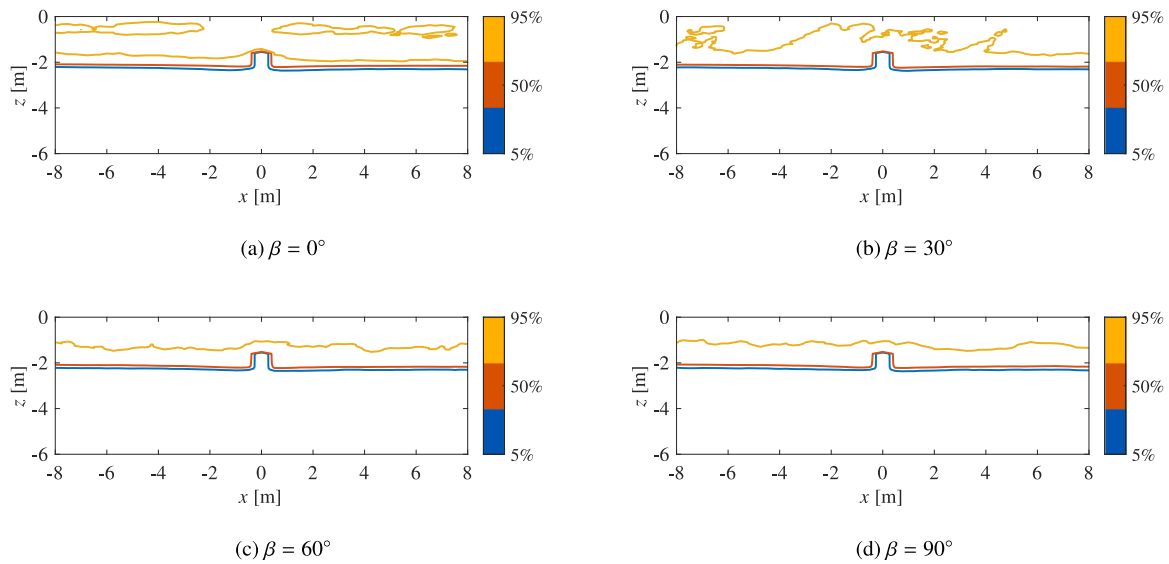


Fig. 7. Probabilistic results, based on the MCSs, of the liquefaction fields during one complete wave period for the cases of heterogeneous hydraulic conductivity fields with different rotation angles.

above the pipeline are liquefied. The liquefaction zone is limited within the seabed surface vicinity with depth as deep as approximately -2 m and a width of approximately 40 m. The boundary of the liquefaction zone shows some winding details (e.g., Figs. 6b and 6c), which might be a result of the soil heterogeneity effects. Besides that, there is no observable patterns in the liquefaction profiles with the increase of rotation angle. Further investigations on liquefaction will be made based on the results of the MCSs.

Based on the results of the MCSs, the probability of liquefaction at every location of the seabed is evaluated. The contour maps of the liquefaction probability during a complete wave period are depicted in Fig. 7. In this case, only the results near the pipeline are shown to get a better view of the seabed response around the pipeline. The contour maps are obtained as follows. First, a grid of points that overlap the entire seabed is created. Then, following the criterion defined in Eq. (17), the liquefaction state at every grid point in every MCS is evaluated. The liquefaction state is denoted as yes if the location could liquefy anytime with the progressive of wave. Lastly, the probability of liquefaction at each grid point is obtained by counting the total number of liquefactions at this point based on the results of all 500 MCSs, and the contour maps are plotted. With an increase in the rotation angle, the area of the region with a 95% probability of liquefaction (i.e., the area enclosed by the 95% contour) decreases. There are fairly significant winding details in the liquefaction profiles when rotation angles are small (e.g.,  $\beta = 0^\circ$  and  $30^\circ$ ), indicating a more complex liquefaction situation in these cases.

As a qualitative analysis of the liquefaction situations, the area of the liquefied region at a particular time in each MCS is calculated. It is worth noting that due to the heterogeneity of the seabed properties, the liquefaction profile, as well as the liquefaction depth, may vary as the wave progresses. Thus, in this work, the liquefied area is chosen as the indicator of the seabed response and is analyzed to gain insights into the liquefaction situation around the pipeline. Fig. 8 plots the statistical results of the liquefied area at time  $t = 3$  s based on the results of all 500 MCSs. As a comparison, the liquefied area for the deterministic case is also plotted. The mean liquefied area of the probabilistic cases is considerably larger (by approximately 11%~16%) than the liquefied area of the deterministic case, and it decreases slightly with the increase of rotation angle. The uncertainty in the liquefied area decreases with increasing rotation angle, which can be identified by observing the heights of the boxes and the heights of the whiskers in the boxplots. The distributions of the liquefied area are skewed to the upper side,

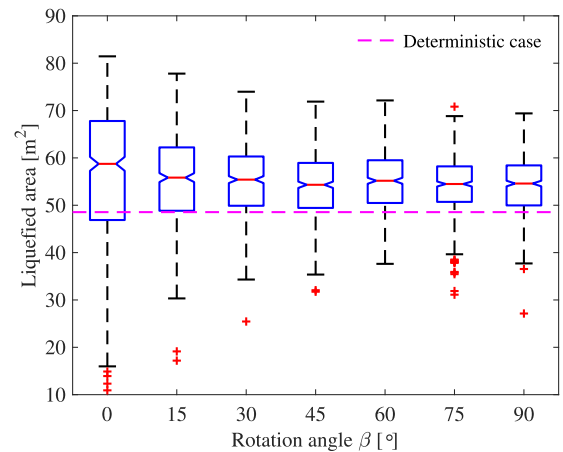


Fig. 8. Relationship between the liquefied area and the rotation angle at time  $t = 3$  s for the cases of heterogeneous hydraulic conductivity. In each box, the central mark indicates the median, and the bottom and top edges of the box indicate the 25th and 75th percentiles, respectively. The whiskers extend to the most extreme data points not considered outliers, and the outliers are plotted individually using the '+' symbol. The whiskers are set to 1.5 times the interquartile range, which corresponds to approximately 99.3 percent coverage if the data were normally distributed. The pink dashed line indicates the liquefied area in the deterministic case.

with a considered number of “outliers” (i.e., the cases out of the 99.3% probability) on the lower side. This phenomenon indicates that situations with small liquefied area values are less likely to occur. As the design of seabed pipelines is generally referring to the most dangerous cases (i.e., the upper bounds of the liquefied area in this example), the results in Fig. 8 indicate that the liquefaction situation of seabed-pipeline would get less severe with increasing rotation angles. The upper bound of liquefied area decreases by approximately 15% with the rotation angle increasing from  $0^\circ$  to  $90^\circ$ .

#### 4.2.2. Seabed displacements

Next, the seabed displacements are analyzed. Figs. 9 and 10 present the horizontal and vertical displacements of the seabed at time  $t = 3$  s for the cases of heterogeneous hydraulic conductivity fields with different rotation angles. The horizontal displacement fields are presented with negative values on the right half and positive values on the



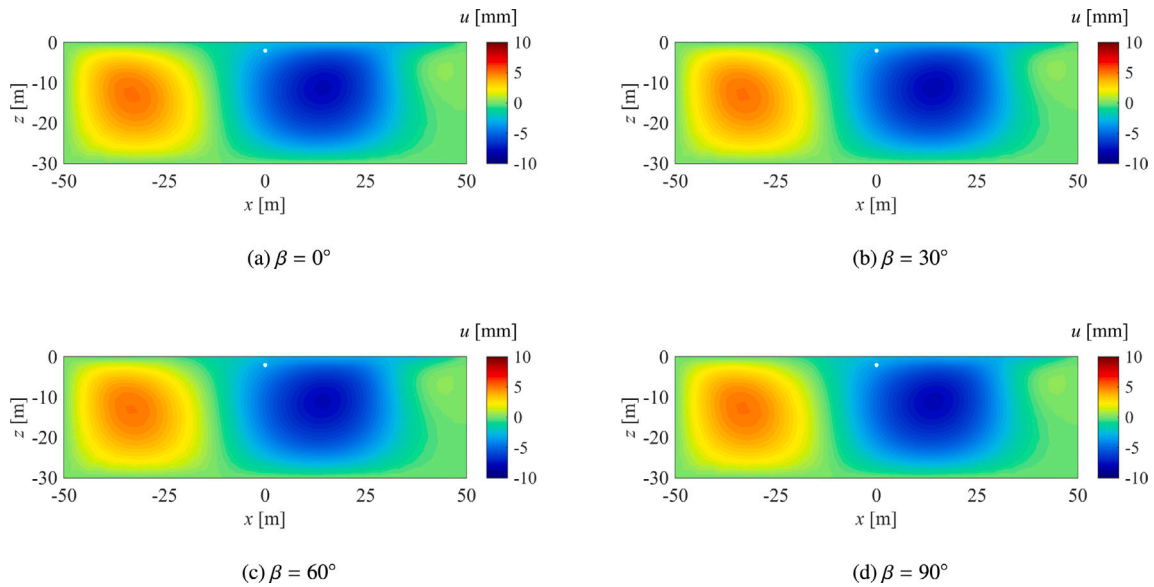


Fig. 9. Contours of the horizontal displacement fields at time  $t = 3$  s for the cases of heterogeneous hydraulic conductivity fields with different rotation angles.

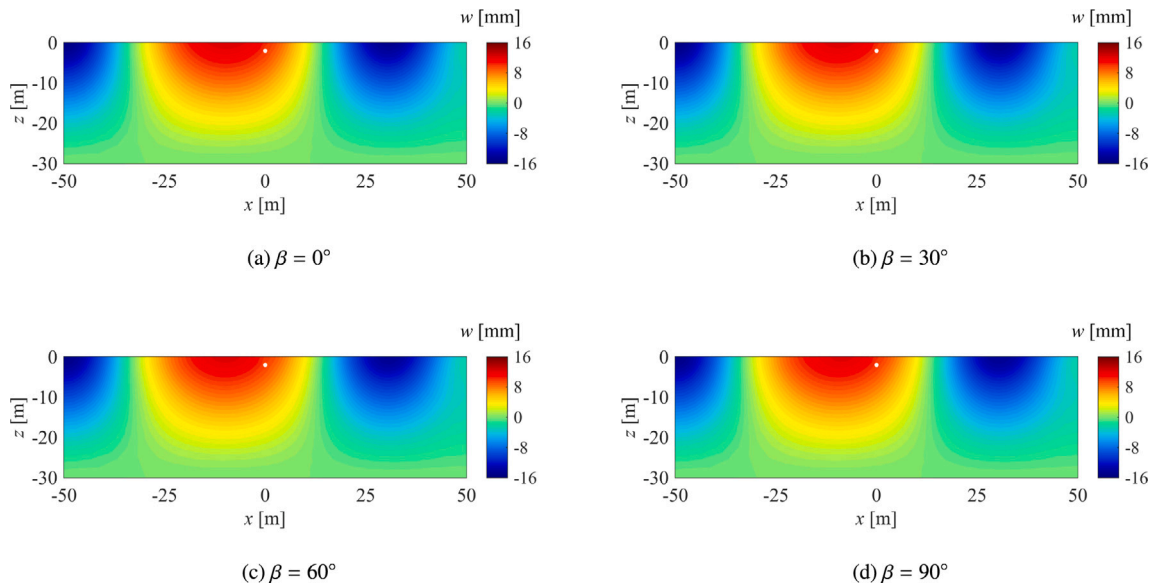


Fig. 10. Contours of the vertical displacement fields at time  $t = 3$  s for the cases of heterogeneous hydraulic conductivity fields with different rotation angles.

left side. On either side, the horizontal displacement magnitudes peak in the central area and diminish towards the boundary. The vertical displacement fields show positive values under the wave troughs and negative values under the wave crests. The magnitude of the vertical displacement is largest at the seabed surface and diminishes with depth. The rotated anisotropy has no noticeable impact on the distribution patterns of the seabed displacements.

To quantitatively investigate the effects of rotated anisotropy on seabed displacements, the displacements at a location right above the top of the pipeline with coordinates  $x = 0$  m and  $z = -1.5$  m are probed. Fig. 11 plots the maximum displacements at this location during one complete wave period for the cases of different rotation angles. For the horizontal displacement, the mean value of the probabilistic cases is smaller (by approximately 1% though) than the value of the deterministic case, and the variation is small with increasing rotation angle. The variation of the displacement uncertainty is also relatively small for different rotation angles. Regarding the vertical displacement, the mean value is greater (by approximately 1%) than the value of the

deterministic case, and it decreases slightly with the rotation angle. The uncertainty first slightly increases and then decreases with increasing rotation angle. For both the horizontal and vertical displacements, the variations in the upper bounds (i.e., the 99.3% upper whiskers) with increasing rotation angles are fairly small (less than 2%).

#### 4.2.3. Pipeline stresses

The stresses in the pipeline due to waves are important matrices for the engineering design of pipelines. Fig. 12 shows the contours of the von Mises stress fields in the pipeline for the cases of heterogeneous hydraulic conductivity with different rotation angles. Overall, the distributions of the von Mises stress for different rotation angles are similar. The top, bottom, left and right parts of the pipeline are subject to high von Mises stresses. With the results of the von Mises stresses, the maximum von Mises stresses experienced by the pipeline during one complete wave period are calculated. Fig. 13 shows the relation between the maximum von Mises stress and the rotation angle. For all the rotation angles, the mean of the maximum von Mises stress is

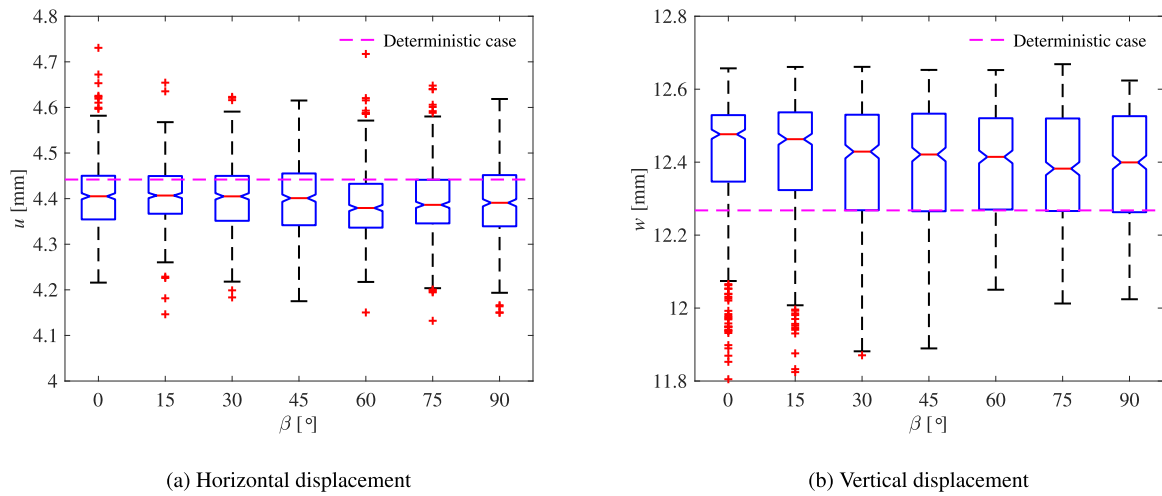


Fig. 11. Relation between the maximum displacement during one complete wave period at the location (0, -1.5) and the rotation angle for the cases of heterogeneous hydraulic conductivity.

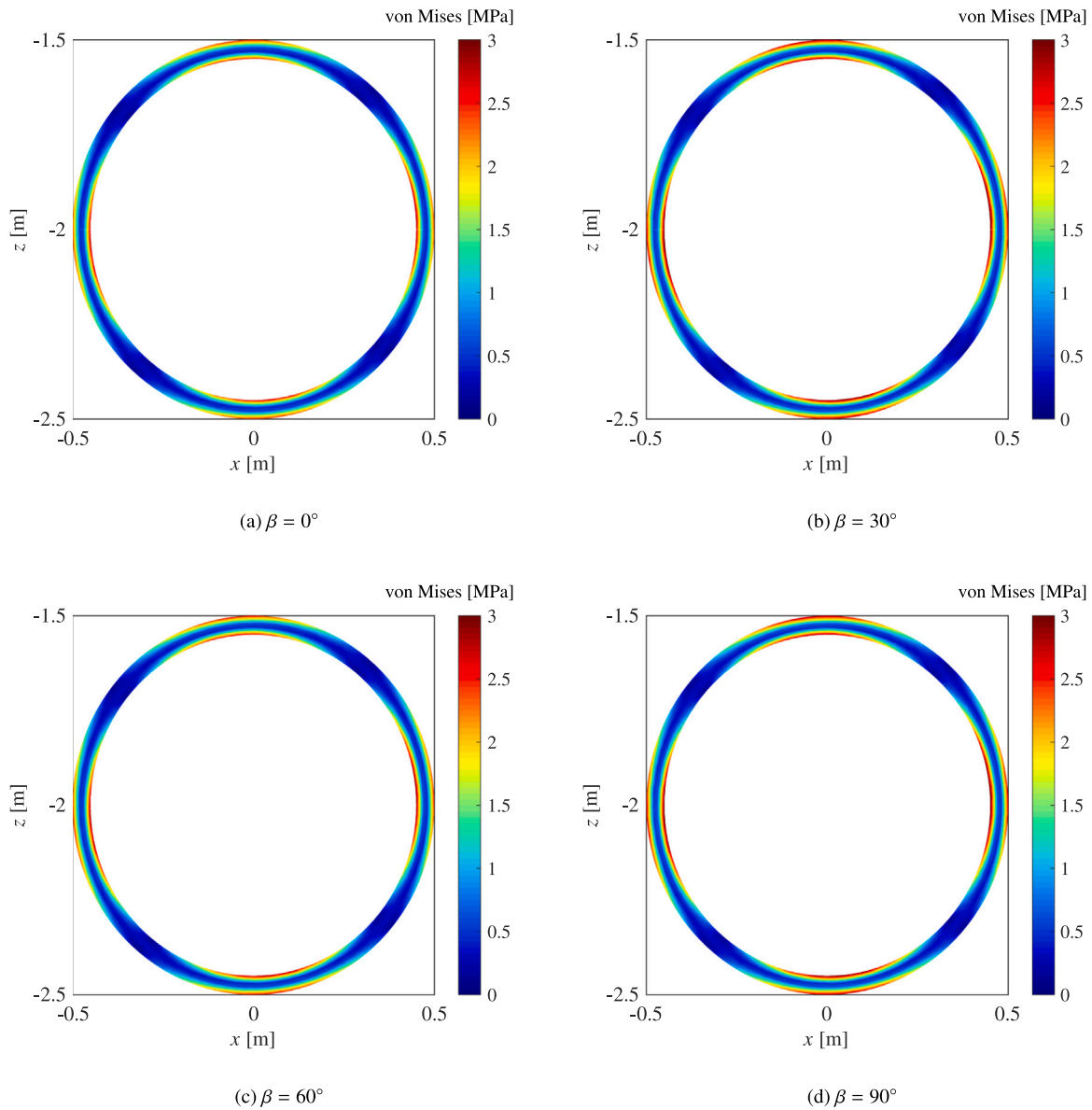


Fig. 12. Contours of the pipeline von Mises stress fields at time  $t = 3$  s for the cases of heterogeneous hydraulic conductivity fields with different rotation angles.

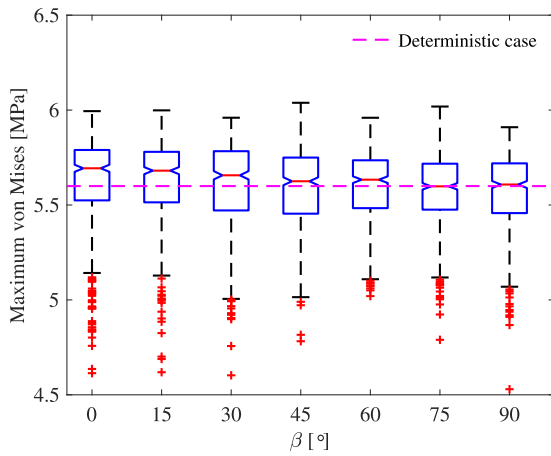


Fig. 13. Relation between the maximum von Mises stress in the pipeline during one complete wave period and the rotation angle for the cases of heterogeneous hydraulic conductivity.

slightly greater (less than 2%) than the maximum von Mises stress of the deterministic case, and it decreases with increasing rotation angle. The uncertainty, in terms of COV, decreases slightly with increasing rotation angle. Together with the results of liquefaction and seabed displacements, it is found that the seabed–pipeline responses would get slightly better with increasing rotated anisotropy in the hydraulic conductivity fields and the transverse anisotropy (i.e., rotation angle  $\beta = 0^\circ$ ) is a most unfavorable situation.

#### 4.3. Effects of rotated anisotropic shear modulus field

Similar to the analysis regarding the rotated anisotropic heterogeneous hydraulic conductivity performed in the previous section, this section reports the results of the rotated anisotropic heterogeneous shear modulus. Based on the statistics described in Section 4.1, heterogeneous shear modulus fields with different rotation angles are generated, and typical realizations are presented in Fig. 14. These shear modulus fields show clear layered profiles with bedding orientations aligned with the specified rotation angles.

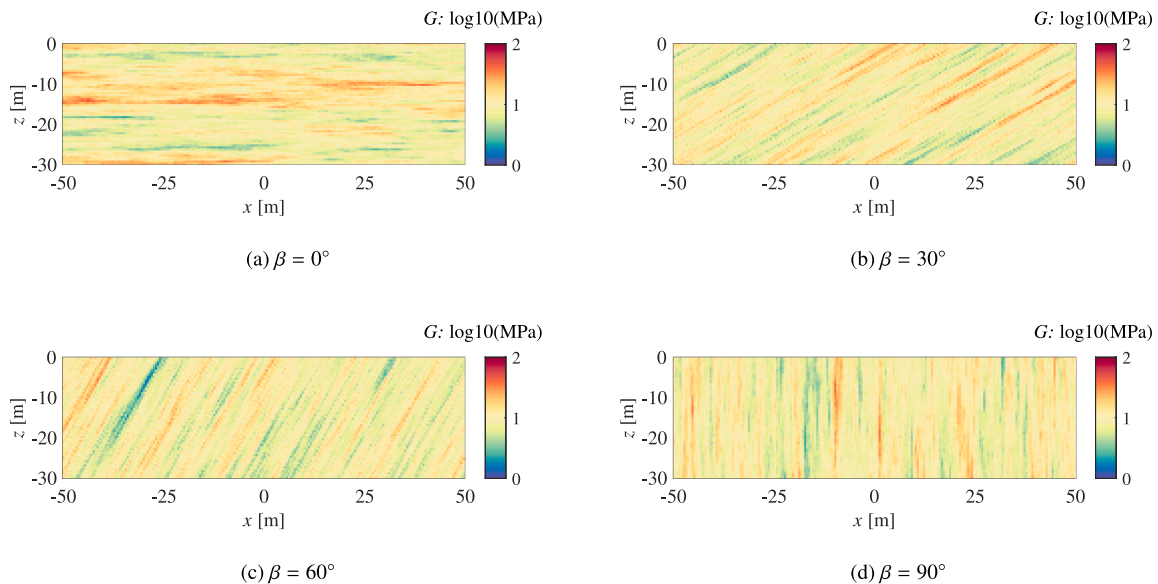


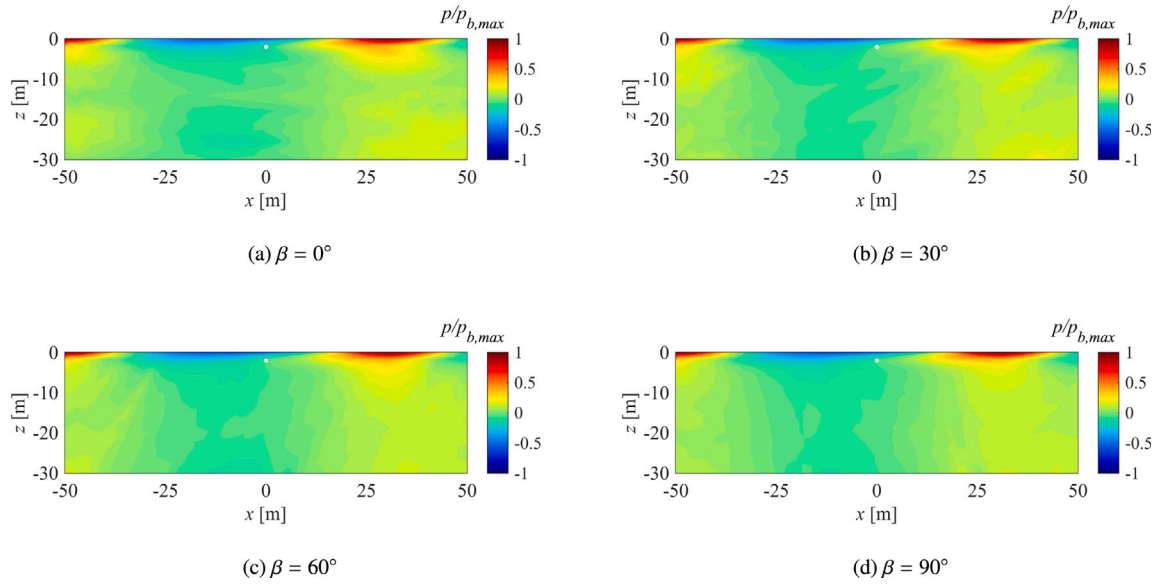
Fig. 14. Typical random field realizations of the seabed shear modulus fields for different rotation angles.

#### 4.3.1. Pore pressure and liquefaction

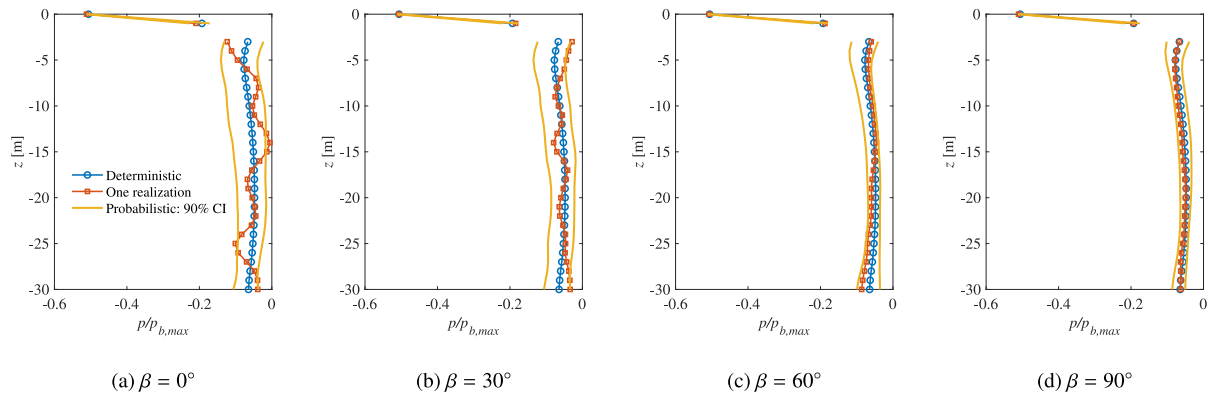
Corresponding to the realizations of shear modulus fields shown in Fig. 14, the results of the excess pore pressure fields at time  $t = 3$  s are presented in Fig. 15. Similar to the hydraulic conductivity cases, the areas with large magnitudes of excess pore pressure are concentrated within approximately 2.5 m below the seabed top surface. The excess pore pressure fields for the cases of different rotation angles exhibit similar patterns, indicating that the rotated anisotropy would not make a significant difference in the pore pressure distribution profiles. Fig. 16 shows the probabilistic results of the excess pore pressure along the vertical cutline  $x = 0$  m based on the 500 MCSs. For all the rotation angles, the excess pore pressure diminishes quickly within the top 2.5 m of the seabed and then varies slowly below this depth. With the increase in the rotation angle, the uncertainty in the excess pore pressure at a particular depth decreases. When the rotation angle increases to  $90^\circ$  (i.e., the bedding orientation becomes vertically aligned), the uncertainty becomes relatively insignificant, and the excess pore pressure of the heterogeneous cases almost coincides with that of the homogeneous case.

Fig. 17 shows the contours of the liquefaction fields at time  $t = 3$  s for different rotation angles. Again, at this particular time, the liquefaction zone concentrates in the top-middle region of the seabed that surrounds the pipeline. The liquefaction zones for all four rotation angles exhibit similar profiles, with the boundaries smoother than those of the heterogeneous hydraulic conductivity cases (comparing with the results shown in Fig. 6). The probabilistic results of the liquefaction zone for a complete wave period are depicted in Fig. 18. With the increase in rotation angle, the area of the region where the liquefaction state is uncertain (with a probability between 5% and 95%) decreases slightly. This phenomenon is consistent with observations made from the results of excess pore pressure (Fig. 15), as expected from relation Eq. (17), that the uncertainty in the excess pore pressure diminishes with increasing rotation angle.

Fig. 19 shows the relation between the liquefied area and the rotation angles at time  $t = 3$  s. In all cases, the mean of the liquefied area of the probabilistic case is smaller than the liquefied area of the deterministic case. With an increase in the rotation angle, the mean of the liquefied area increases and approaches asymptotically towards the value of the deterministic case. Regarding the uncertainty in the liquefied area, there is a clear trend that the uncertainty decreases with increasing rotation angle. The COV decreases from approximately 0.11 to 0.04 with the rotation angle increasing from  $0^\circ$  to  $90^\circ$ . For the upper



**Fig. 15.** Contours of the normalized excess pore pressure fields at time  $t = 3$  s for the cases of heterogeneous shear modulus fields with different rotation angles.



**Fig. 16.** Distributions of excess pore pressure along the vertical cutline  $x = 0$  at time  $t = 3$  for the deterministic and heterogeneous shear modulus fields (90% confidence interval shown) with different rotation angles.

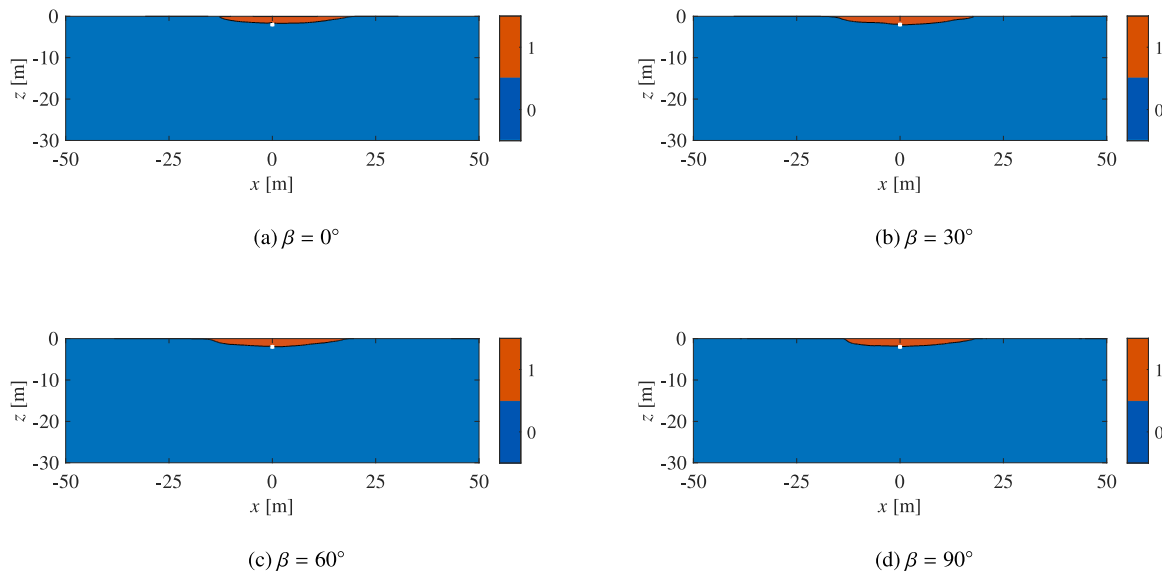


**Fig. 17.** Contours of the liquefaction fields at time  $t = 3$  s for the cases of heterogeneous shear modulus fields with different rotation angles.



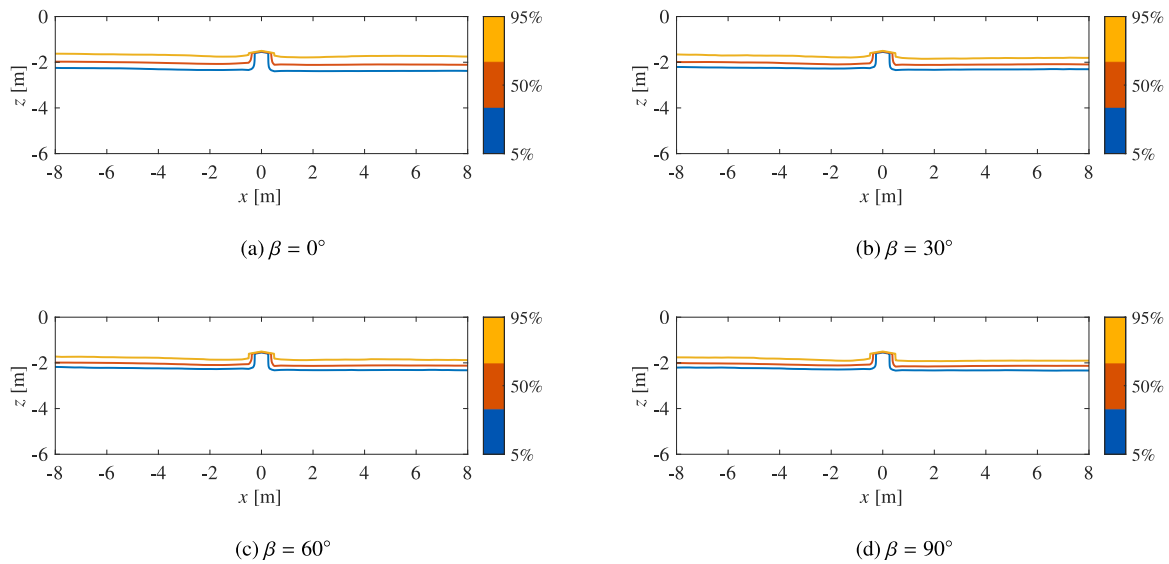


Fig. 18. Probabilistic results of the liquefaction fields during one complete wave period for the cases of heterogeneous shear modulus fields with different rotation angles.

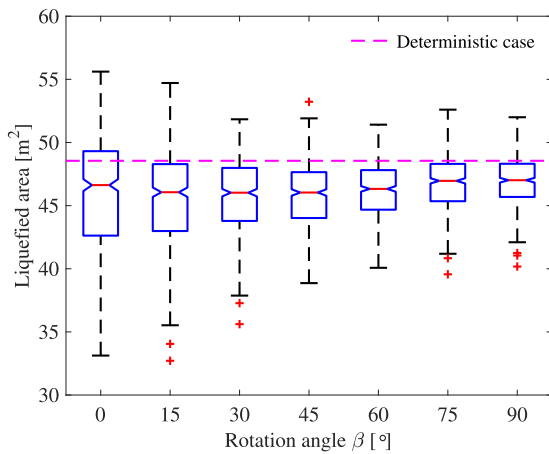


Fig. 19. Relationship between the liquefied area and the rotation angle at time  $t = 3$  s for the cases of heterogeneous shear moduli.

bound of the liquefied area, it decreases by approximately 8% with the rotation angle increase from  $0^\circ$  to  $30^\circ$  and then show less significant variations with the rotation angle increase from  $30^\circ$  to  $90^\circ$ .

#### 4.3.2. Seabed displacements

Figs. 20 and 21 present the horizontal and vertical displacement fields, respectively, of the seabed for different rotation angles. In all cases, the horizontal and vertical displacement fields exhibit almost the same profiles. The MCS results of the maximum displacements right at the top of the pipeline during one complete wave period are plotted in Fig. 22. For both the horizontal and vertical displacements, their mean values are overall greater (by approximately 10% on average) than the results of the deterministic case. There is a trend that the mean values of the horizontal and vertical displacements, respectively, first slightly increase and then decrease with the increase of rotation angle. The uncertainty in the horizontal and vertical displacements due to heterogeneous shear modulus is significantly larger than that due to heterogeneous hydraulic conductivity (comparing Fig. 22 with Fig. 11). The COV of the horizontal displacement decreases by approximately 25% with the rotation angle increasing from  $0^\circ$  to  $90^\circ$ , while the COV of the vertical displacement varies within 10% for different rotation angles.

#### 4.3.3. Pipeline stresses

Fig. 23 shows the contours of the pipeline von Mises stress field at time  $t = 3$  s. The results indicate that the rotated anisotropy in the shear modulus does not impact the distribution patterns of the von Mises stress fields in the pipeline. The maximum von Mises stress in the pipeline during one complete wave period for the cases of different rotation angles are shown in Fig. 24. Overall, the mean of the maximum von Mises stress of the probabilistic cases are all fairly close to the maximum von Mises stress of the deterministic case. The uncertainties in the maximum von Mises stresses of the heterogeneous shear modulus cases are significantly greater than those of the heterogeneous hydraulic conductivity cases, by comparing with the results of the hydraulic conductivity cases shown in Fig. 13. With an increase in the rotation angle, the uncertainty first decreases and then increases. The uncertainty in the maximum von Mises stress is minimal when the rotation angle is approximately  $45^\circ$ . The upper bound of the maximum von Mises stresses with the rotation angle at  $45^\circ$  would be as much as 20% less than that with the rotation angle at  $0^\circ$  or  $90^\circ$ . Together with the results of liquefaction and seabed displacements, it is found that the overall seabed-pipeline responses would get slightly better with increasing rotated anisotropy in the shear modulus field. The transverse anisotropy is the most unfavorable situation and the rotated anisotropy with rotation angle at about  $45^\circ$  is the most favorable one.

### 5. Conclusion

In this work, a probabilistic analysis on seabed-pipelines is performed to investigate the effects of rotated anisotropy in seabed properties on the hydromechanical responses of seabed-pipelines under dynamic wave-induced loadings. Random field hydraulic conductivity and shear moduli with different rotation angles are generated and imported into the hydromechanical FEM model with which the seabed-pipeline responses are solved. Based on the results of MCSs, the pore pressure, liquefaction, seabed displacement, and pipeline von Mises stresses are analyzed in a probabilistic fashion. The main findings of this work are as follows:

1. The overall distribution profiles of the pore pressure, liquefaction, seabed displacement, and pipeline von Mises stresses are not affected much by the heterogeneity of and rotated anisotropy in the hydraulic conductivity and shear modulus. The effects of rotated anisotropic heterogeneous hydraulic conductivity and shear modulus could be reflected by the analyzed quantitative matrices.

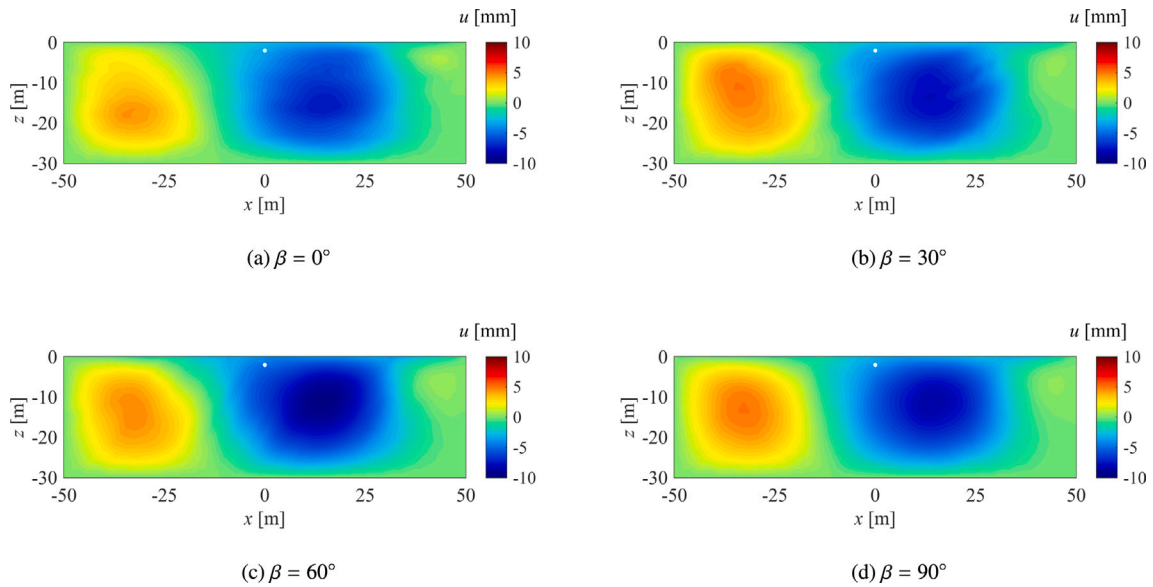


Fig. 20. Contours of the horizontal displacement fields at time  $t = 3$  s for the cases of heterogeneous shear modulus fields with different rotation angles.

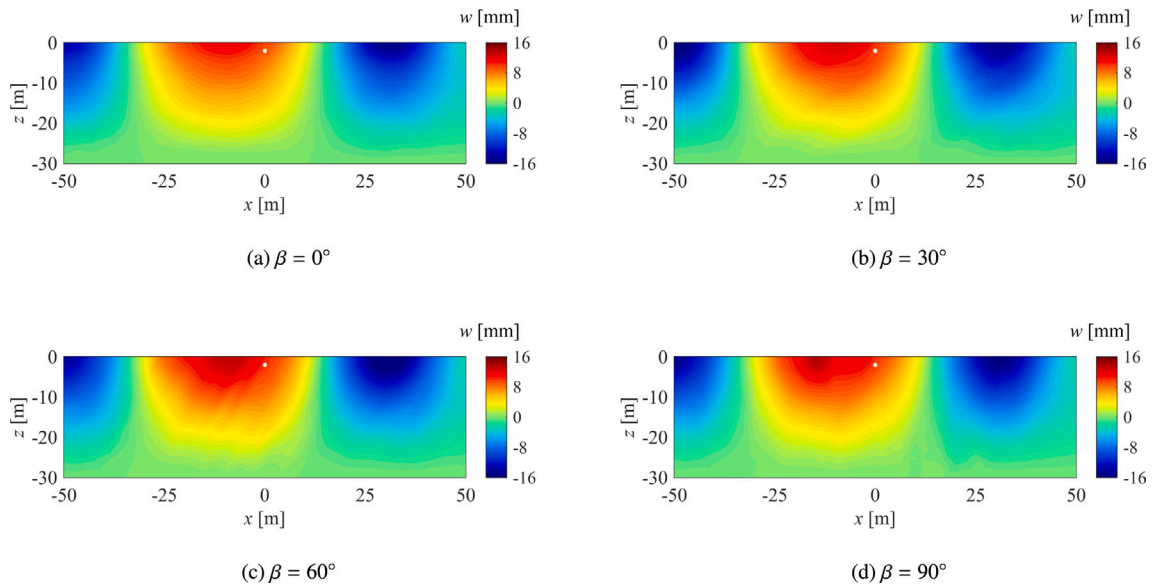


Fig. 21. Contours of the vertical displacement fields at time  $t = 3$  s for the cases of heterogeneous shear modulus fields with different rotation angles.

- Based on MCS, the mean of and the uncertainty in the liquefied areas decrease noticeably with the increasing rotated anisotropy in hydraulic conductivity. For shear modulus, the mean first decreases and then increases but the uncertainty decreases monotonically with increasing rotated anisotropy. In terms of the upper bounds of the liquefied area (referring to the most dangerous case for engineering design), the variations due to the rotated anisotropy effects could be as much as 15% for hydraulic conductivity and 8% for shear modulus.
- The variations in seabed displacements due to the increasing rotated anisotropy in hydraulic conductivity are relatively small, and they are within 2% in terms of the upper bounds of the seabed displacements. With increasing rotated anisotropy in shear modulus, the mean of the seabed displacements first increases and then decreases (with the inflection point at about  $45^\circ$ ). The COV in the horizontal displacement decreases by approximately 25% with increasing rotation angle, while it varies within 10% for the vertical displacement.
- For hydraulic conductivity, both the mean of and the uncertainty in the maximum von Mises stresses in the pipeline decrease (by less than 2% though) with the increasing rotated anisotropy. As to shear modulus, the mean slightly increases, while the uncertainty first decreases and then increases, with increasing rotated anisotropy. The variations in the upper bounds for different rotation angles could be as much as 20% and the upper bound is minimal when the rotation angle is approximately  $45^\circ$ .
- Overall, the transverse anisotropy in hydraulic conductivity or shear modulus is the most unfavorable situation. The seabed–pipeline behavior generally gets “better” with the increase of rotated anisotropy in hydraulic conductivity. And, for shear modulus, it gets “better” with the rotation angle changing from  $0^\circ$  or  $90^\circ$  to  $45^\circ$  (i.e.,  $45^\circ$  is a most favorable situation). If the rotated anisotropy of a seabed property is unknown in a field project, the analysis with transverse anisotropy could be relied upon for conservative design.

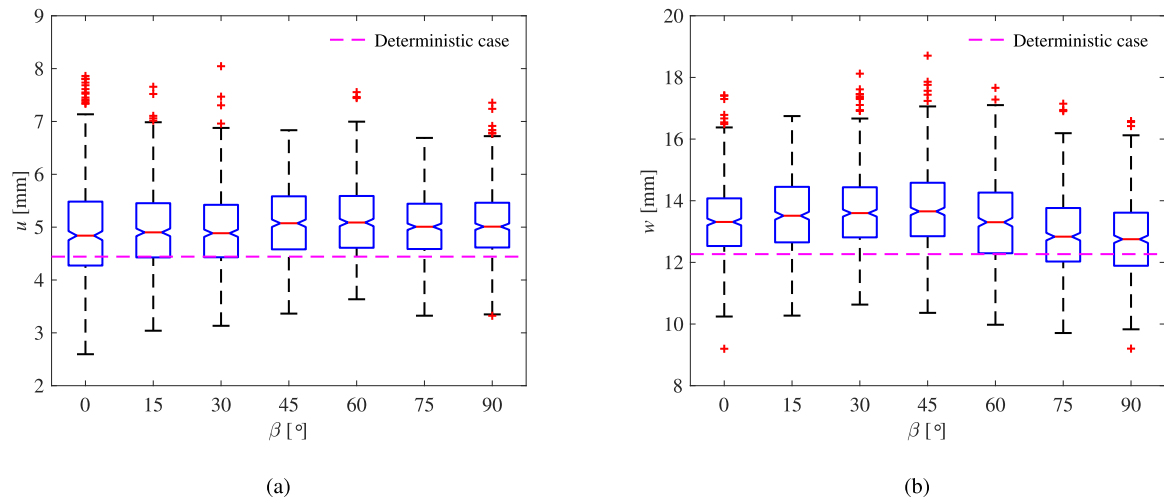


Fig. 22. Relation between the maximum displacements during one complete wave period at the location (0, -1.5) and the rotation angle for the cases of heterogeneous shear moduli.

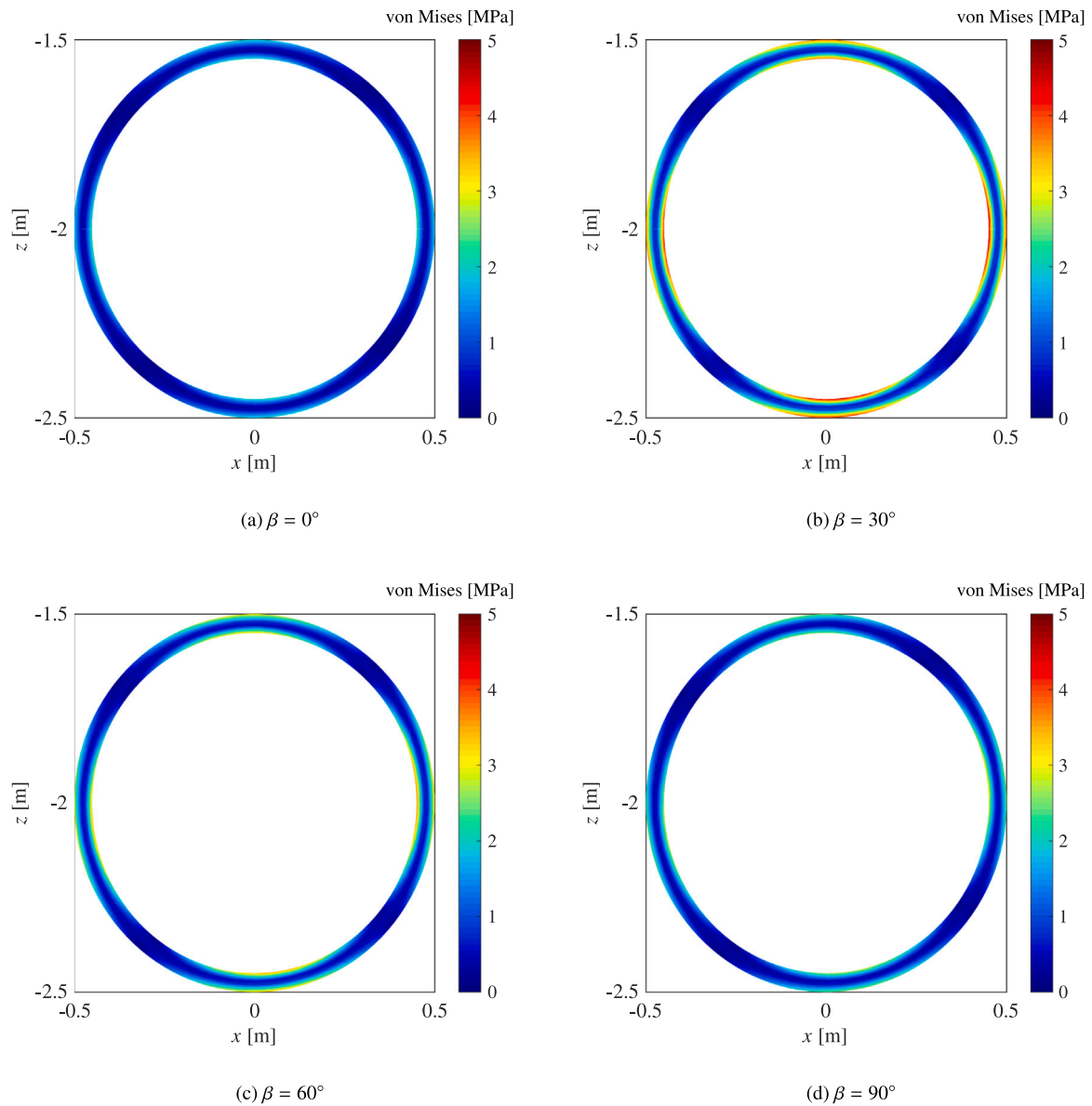


Fig. 23. Contours of the pipeline von Mises stress fields at time  $t = 3$  s for the cases of heterogeneous shear modulus fields with different rotation angles.

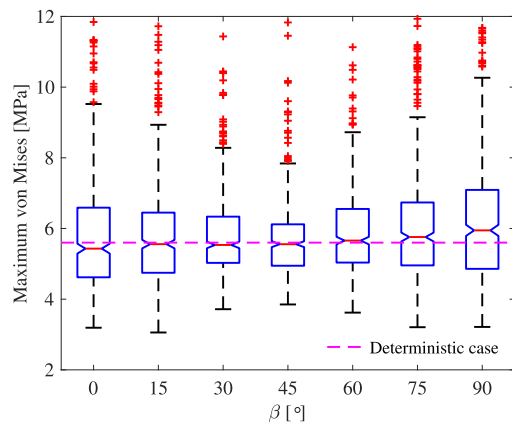


Fig. 24. Relation between the maximum von Mises stress in the pipeline during one complete wave period and the rotation angle for the cases of heterogeneous shear moduli.

Lastly, it is noted that the influence of the degree of saturation on the seabed–pipeline may be comparable to the hydraulic conductivity and shear modulus (Hsu and Jeng, 1994; Jeng, 2012). Additional simulations with different extents of rotated anisotropy in the degree of saturation are also conducted, while the results are not presented herein. It is found that with adopted parameters of degree of saturation (i.e., random field degree of saturation in the range of 0.96–0.99), the effects of rotated anisotropy in degree of saturation on the seabed–pipeline responses are fairly small. And, similar to the conclusions of the hydraulic conductivity and shear modulus cases, the transverse anisotropy in degree of saturation is also the most unfavorable situation.

#### CRedit authorship contribution statement

**Zhengshou Lai:** Conceptualization, Methodology, Software, Validation, Writing - original draft. **Qiushi Chen:** Conceptualization, Methodology, Writing - review & editing, Supervision. **Linchong Huang:** Writing - review & editing, Funding acquisition, Supervision.

#### Declaration of competing interest

The authors declare that they have no known competing financial interests or personal relationships that could have appeared to influence the work reported in this paper.

#### Acknowledgments

The first author would like to acknowledge the support by the Hong Kong Scholars Program (2020). Both the first and third authors would like to acknowledge the support by the Fundamental Research Funds for the Central Universities, China (grant no. 19lgpy289), the National Natural Science Foundation of China (51909289, 51978677), the China Postdoctoral Science Foundation (grant no. 2019M663240), and the Shenzhen Natural Science Foundation (grant no. JCYJ20190807162401662).

#### References

Allaix, D.L., Carbone, V.I., 2009. Discretization of 2D random fields: A genetic algorithm approach. *Eng. Struct.* 31, 1111–1119.  
 Chen, Q., Seifried, A., Andrade, J.E., Baker, J.W., 2012. Characterization of random fields and their impact on the mechanics of geosystems at multiple scales. *Int. J. Numer. Anal. Methods Geomech.* 36, 140–165.  
 Chen, Q., Wang, C., Juang, C.H., 2016a. Cpt-based evaluation of liquefaction potential accounting for soil spatial variability at multiple scales. *J. Geotech. Geoenviron. Eng.* 142, 04015077.

Chen, Q., Wang, C., Juang, C.H., 2016b. Probabilistic and spatial assessment of liquefaction-induced settlements through multiscale random field models. *Eng. Geol.* 211, 135–149.  
 Chenari, R.J., Farahbakhsh, H.K., 2015. Generating non-stationary random fields of auto-correlated, normally distributed CPT profile by matrix decomposition method. In: *Georisk: Assessment and Management of Risk for Engineered Systems and Geohazards*, Vol. 9. pp. 96–108.  
 Cressie, N., Pavlicová, M., 2002. Calibrated spatial moving average simulations. *Stat. Model.* 2, 267–279.  
 Davis, M.W., 1987. Production of conditional simulations via the LU triangular decomposition of the covariance matrix. *Math. Geol.* 19, 91–98.  
 Fenton, G.A., Vanmarcke, E.H., 1990. Simulation of random fields via local average subdivision. *J. Eng. Mech.* 116, 1733–1749.  
 Griffiths, D.V., Schiermeyer, R.P., Huang, J., Fenton, G.A., 2009. Influence of anisotropy and rotation on probabilistic slope stability analysis by RFEM. In: *Proceedings of GeoHalifax*. pp. 542–546.  
 Hsu, H., Chen, Y., Hsu, J.R.C., Tseng, W., 2009. Nonlinear water waves on uniform current in Lagrangian coordinates. *J. Nonlinear Math. Phys.* 16, 47–61.  
 Hsu, J.R.C., Jeng, D.S., 1994. Wave-induced soil response in an unsaturated anisotropic seabed of finite thickness. *Int. J. Numer. Anal. Methods Geomech.* 18, 785–807.  
 Hsu, J.R.C., Jeng, D.S., Lee, C.P., 1995. Oscillatory soil response and liquefaction in an unsaturated layered seabed. *Int. J. Numer. Anal. Methods Geomech.* 19, 825–849.  
 Jeng, D.S., 2012. *Porous Models for Wave-Seabed Interactions*. Springer Science & Business Media.  
 Jeng, D.S., Lin, Y., 1999. Pore pressure on a submarine pipeline in a cross-anisotropic nonhomogeneous seabed under water-wave loading. *Can. Geotech. J.* 36, 563–572.  
 Jeng, D.S., Seymour, B.R., 1997. Response in seabed of finite depth with variable permeability. *J. Geotech. Geoenviron. Eng.* 123, 902–911.  
 Jiang, S., Li, D., Cao, Z., Zhou, C., Phoon, K., 2014. Efficient system reliability analysis of slope stability in spatially variable soils using Monte Carlo simulation. *J. Geotech. Geoenviron. Eng.* 141, 04014096.  
 Lai, Z., Chen, Q., Wang, C., Zhou, X., 2019. Modeling dynamic responses of heterogeneous seabed with embedded pipeline through multiresolution random field and coupled hydromechanical simulations. *Ocean Eng.* 173, 556–570.  
 Lai, C., Xie, M., Murthy, D., 2003. A modified Weibull distribution. *IEEE Trans. Reliab.* 52, 33–37.  
 Leung, Y.F., Liu, W., Li, J.S., Wang, L., Tsang, D.C.W., Lo, C.Y., Leung, M.T., Poon, C.S., 2018. Three-dimensional spatial variability of arsenic-containing soil from geogenic source in Hong Kong: Implications on sampling strategies. *Sci. Total Environ.* 633, 836–847.  
 Liao, C., Tong, D., Jeng, D.S., Zhao, H., 2018. Numerical study for wave-induced oscillatory pore pressures and liquefaction around impermeable slope breakwater heads. *Ocean Eng.* 157, 364–375.  
 Liu, W., Chen, Q., Wang, C., Juang, C.H., Chen, G., 2017. Spatially correlated multiscale Vs30 mapping and a case study of the Suzhou site. *Eng. Geol.* 220, 110–122.  
 Liu, W.F., Leung, Y.F., 2018. Characterising three-dimensional anisotropic spatial correlation of soil properties through in situ test results. *Géotechnique* 68, 805–819.  
 Maâtoug, M.A., Ayadi, M., 2016. Numerical simulation of the second-order Stokes theory using finite difference method. *Alexandria Eng. J.* 55, 3005–3013.  
 Ou, J., 2009. *Three-Dimensional Numerical Modelling of Interaction Between Soil and Pore Fluid* (Ph.D. thesis). University of Birmingham.  
 Pastor, M., Chan, A.H.C., Mira, P., Manzanal, D., Fernández Merodo, J.A., Blanc, T., 2011. Computational geomechanics: the heritage of Olek Zienkiewicz. *Internat. J. Numer. Methods Engrg.* 87, 457–489.  
 Peng, X., Zhang, L., Jeng, D.S., Chen, L., Liao, C., Yang, H., 2017. Effects of cross-correlated multiple spatially random soil properties on wave-induced oscillatory seabed response. *Appl. Ocean Res.* 62, 57–69.  
 Qi, W., Gao, F., 2018. Wave induced instantaneously-liquefied soil depth in a non-cohesive seabed. *Ocean Eng.* 153, 412–423.  
 Rehfeldt, K.R., Boggs, J.M., Gelhar, L.W., 1992. Field study of dispersion in a heterogeneous aquifer: 3. geostatistical analysis of hydraulic conductivity. *Water Resour. Res.* 28, 3309–3324.  
 Sharqawy, M.H., Lienhard, J.H., Zubair, S.M., 2010. Thermophysical properties of seawater: a review of existing correlations and data. *Desalination Water Treat.* 16, 354–380.  
 Shen, M., Juang, C.H., Chen, Q., 2019. Mitigation of liquefaction hazard by dynamic compaction – a random field perspective. *Can. Geotech. J.* 56, 1803–1815.  
 Sudret, B., Der Kiureghian, A., 2000. *Stochastic Finite Element Methods and Reliability: A State-of-the-Art Report*. Department of Civil and Environmental Engineering, University of California, Berkeley.  
 Sui, T., Jin, Y., Wang, Z., Zhang, C., Shi, J., 2019. Effects of the soil property distribution gradient on the wave-induced response of a non-homogeneous seabed. *J. Mar. Sci. Eng.* 7, 281.  
 Sui, T., Zhang, C., Zheng, J., Guo, Y., Xie, M., 2018. Numerical study of standing wave-induced seabed residual response with the non-homogeneous soil property. *J. Coast. Res.* 85, 921–925.  
 Sui, T., Zheng, J., Zhang, C., Jeng, D.S., Zhang, J., Guo, Y., He, R., 2017. Consolidation of unsaturated seabed around an inserted pile foundation and its effects on the wave-induced momentary liquefaction. *Ocean Eng.* 131, 308–321.  
 Sumer, B., 2014. *Liquefaction Around Marine Structures*. World Scientific.



- Tong, D., Liao, C., Jeng, D.S., Zhang, L., Wang, J., Chen, L., 2017. Three-dimensional modeling of wave-structure-seabed interaction around twin-pile group. *Ocean Eng.* 145, 416–429.
- Ülker, M.B.C., 2015. Semianalytical solution to the wave-induced dynamic response of saturated layered porous media. *J. Waterw. Port Coast. Ocean Eng.* 141, 06014001.
- Walton, M., Brothers, D., Miller, D., Conrad, J., Haeussler, P., Kluesner, J., 2018. Expedition along a hazardous, fast-moving fault off southeast Alaska – the Queen Charlotte-Fairweather Fault. URL: <https://archive.usgs.gov/archive/sites/soundwaves.usgs.gov/2018/01/index.html>.
- Wang, C., Chen, Q., 2018. A hybrid geotechnical and geological data-based framework for multiscale regional liquefaction hazard mapping. *Géotechnique* 68, 614–625.
- Weibull, W., 1951. A statistical distribution function of wide applicability. *J. Appl. Mech.* 18, 290–293.
- Yamamoto, T., Suzuki, Y., 1980. Stability analysis of seafloor foundations. In: *Coastal Engineering 1980*. pp. 1799–1818.
- Yang, G., Ye, J., 2017. Wave & current-induced progressive liquefaction in loosely deposited seabed. *Ocean Eng.* 142, 303–314.
- Yang, G., Ye, J., 2018. Nonlinear standing wave-induced liquefaction in loosely deposited seabed. *Bull. Eng. Geol. Environ.* 77, 205–223.
- Ye, J., 2012. 3D liquefaction criteria for seabed considering the cohesion and friction of soil. *Appl. Ocean Res.* 37, 111–119.
- Ye, J.H., Jeng, D.S., 2012. Response of porous seabed to nature loadings: waves and currents. *J. Eng. Mech.* 138, 601–613.
- Ye, J., Wang, G., 2015. Seismic dynamics of offshore breakwater on liquefiable seabed foundation. *Soil Dyn. Earthq. Eng.* 76, 86–99.
- Ye, J., Wang, G., 2016. Numerical simulation of the seismic liquefaction mechanism in an offshore loosely deposited seabed. *Bull. Eng. Geol. Environ.* 75, 1183–1197.
- Zen, K., Yamazaki, H., 1990. Mechanism of wave-induced liquefaction and densification in seabed. *Soils Found.* 30, 90–104.
- Zhang, L., Cheng, Y., Li, J., Zhou, X., Jeng, D.S., Peng, X., 2016a. Wave-induced oscillatory response in a randomly heterogeneous porous seabed. *Ocean Eng.* 111, 116–127.
- Zhang, C., Sui, T., Zheng, J., Xie, M., Nguyen, V.T., 2016b. Modelling wave-induced 3D non-homogeneous seabed response. *Appl. Ocean Res.* 61, 101–114.
- Zhang, Y., Ye, J., He, K., Chen, S., 2019. Seismic dynamics of pipeline buried in dense seabed foundation. *J. Mar. Sci. Eng.* 7, 190.
- Zhao, H., Jeng, D.S., Liao, C., 2016. Effects of cross-anisotropic soil behaviour on the wave-induced residual liquefaction in the vicinity of pipeline buried in elasto-plastic seabed foundations. *Soil Dyn. Earthq. Eng.* 80, 40–55.
- Zhao, K., Xiong, H., Chen, G., Zhuang, H., Du, X., 2017. Cyclic characterization of wave-induced oscillatory and residual response of liquefiable seabed. *Eng. Geol.* 227, 32–42.
- Zhou, M., Jeng, D.S., Qi, W., 2020. A new model for wave-induced instantaneous liquefaction in a non-cohesive seabed with dynamic permeability. *Ocean Eng.* 213, 107597.
- Zhou, X., Wang, J.H., Zhang, J., Jeng, D.S., 2014. Wave and current induced seabed response around a submarine pipeline in an anisotropic seabed. *Ocean Eng.* 75, 112–127.
- Zhou, X., Xu, B., Wang, J., Li, Y., 2011. An analytical solution for wave-induced seabed response in a multi-layered poro-elastic seabed. *Ocean Eng.* 38, 119–129.
- Zhu, B., Pei, H., Yang, Q., 2019a. Reliability analysis of submarine slope considering the spatial variability of the sediment strength using random fields. *Appl. Ocean Res.* 86, 340–350.
- Zhu, H., Zhang, L., 2013. Characterizing geotechnical anisotropic spatial variations using random field theory. *Can. Geotech. J.* 50, 723–734.
- Zhu, H., Zhang, L., Xiao, T., 2019b. Evaluating stability of anisotropically deposited soil slopes. *Can. Geotech. J.* 56, 753–760.